

ELECTROMECHANICAL FILTERS USING
MICROMACHINED COUPLED CIRCULAR
PLATE RESONATORS

A DISSERTATION SUBMITTED TO
THE GRADUATE SCHOOL OF ENGINEERING AND SCIENCE
OF BILKENT UNIVERSITY
IN PARTIAL FULFILLMENT OF THE REQUIREMENTS FOR
THE DEGREE OF
DOCTOR OF PHILOSOPHY
IN
ELECTRICAL AND ELECTRONICS ENGINEERING

By
Muhammed Abdulcelil Acar
September 2021

ELECTROMECHANICAL FILTERS USING MICROMACHINED
COUPLED CIRCULAR PLATE RESONATORS

By Muhammed Abdulcelil Acar

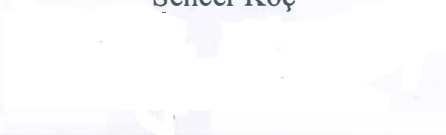
September 2021

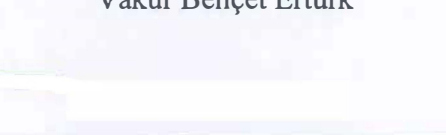
We certify that we have read this dissertation and that in our opinion it is fully adequate, in scope and in quality, as a dissertation for the degree of Doctor of Philosophy.

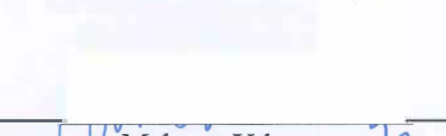

Hayrettin Köymen (Advisor)


Abdullah Atalar (Co-Advisor)


Sencer Koç


Vakur Behçet Ertürk


Barış Bayram


Mehmet Yılmaz

Approved for the Graduate School of Engineering and Science:

 Ezhan Karaşan
Director of the Graduate School

Copyright Information

© 2021 IOP Publishing. Reproduced with permission, from Acar M A, Atalar A, Yilmaz M and Köymen H 2021 Mechanically coupled clamped circular plate resonators: modeling, design and experimental verification *J. Micromech. Microeng.* [31 105002](#). All rights reserved.

ABSTRACT

ELECTROMECHANICAL FILTERS USING
MICROMACHINED COUPLED CIRCULAR PLATE
RESONATORS

Muhammed Abdulcelil Acar
Ph.D. in Electrical and Electronics Engineering
Advisor: Hayrettin Köymen
Co-Advisor: Abdullah Atalar
September 2021

Mechanically coupled resonators fabricated using micromachining usually require a mechanical coupling element; this introduces additional complexity to the picture. We propose a novel modeling and design approach, followed by experimental verification, for mechanically coupled clamped circular plate resonators fabricated using a commercial micromachining process in which no additional coupling element is present. In our study, the flexural mode clamped circular plate resonators overlap to an extent. Their clamps at the overlap region are removed to generate a freely moving coupling boundary between the resonators. The practical measure of the overlap is small enough to preserve the characteristics of each resonator. This result enables modeling the coupled-resonators based on the clamped circular plate resonator model. A physics-based lumped element equivalent circuit model is developed where dimensions, bias voltage, and material properties are controllable variables. Each of the model parameters is expressed as the corresponding single resonator model parameter multiplied by a function of the amount of overlap. Analytical derivations and finite element method (FEM) simulations are used to extract the dependency of the model parameters on the amount of overlap. Closed-form expressions for the coupled-resonator's center frequency, bandwidth, and termination impedance are derived using the developed model. A design procedure is introduced to determine dimensional parameters and bias voltage. The proposed coupled-

resonator offers up to 5% fractional bandwidth. For a typical design using a polysilicon plate with 100 nm gap height, the ratio of the termination impedance to the center frequency is calculated to be 158 Ω /MHz. This result indicates that on-chip intermediate frequency (IF) filters can be implemented at center frequencies up to several hundred MHz using this type of coupled-resonators. A coupled-resonator is designed and realized for a proof of concept demonstration. The measurement results of the coupled-resonator show good agreement with the equivalent circuit model simulations.

Keywords: Circuit modeling, clamped circular plate resonator, coupled-resonators, on-chip IF filter.

ÖZET

KUPLAJLI DAİRESEL MİKROİŞLENMİŞ
REZONATÖRLERİ KULLANAN ELEKTROMEKANİK
FİLTRELER

Muhammed Abdulcelil Acar
Elektrik ve Elektronik Mühendisliği, Doktora
Tez Danışmanı: Hayrettin Köymen
İkinci Tez Danışmanı: Abdullah Atalar
Eylül 2021

Mekanik olarak birleştirilmiş mikroışlenmiş rezonatörler genellikle mekanik bir bağlantı elemanı gerektirir; bu durum yapının tasarımına ek bir karmaşıklık getirir. Ek bir bağlantı elemanının bulunmadığı, ticari bir mikroışleme prosesi kullanılarak üretilen, mekanik olarak birleştirilmiş kenetlenmiş dairesel plaka rezonatörleri için deneysel olarak doğrulanan yeni bir modelleme ve tasarım yaklaşımı öneriyoruz. Çalışmamızda, eğilme modlu kenetlenmiş dairesel plaka rezonatörleri bir dereceye kadar örtüşür ve örtüşme bölgesindeki kelepçeleri, rezonatörler arasında serbestçe hareket eden bir kuplaj bölgesi oluşturmak için çıkarılır. Örtüşmenin miktarı, her bir rezonatörün özelliklerini koruyacak kadar küçüktür. Bu sonuç, birleştirilmiş rezonatörlerin kenetlenmiş dairesel plaka rezonatör modeline dayalı olarak modellenmesini sağlar. Boyutların, öngerilim voltajının ve malzeme özelliklerinin kontrol edilebilir değişkenler olduğu fizik tabanlı bir eşdeğer devre modeli geliştirilmiştir. Model parametrelerinin her biri, örtüşme miktarının bir fonksiyonu ile çarpılan yekpare rezonatör model parametresi ile ifade edilir. Model parametrelerinin örtüşme miktarı ile nasıl değiştiğini ortaya çıkarmak için analitik türetimler ve sonlu elemanlar yöntemi (FEM) simülasyonları kullanılır. Geliştirilen model kullanılarak, birleştirilmiş rezonatörlerin merkez frekansını, bant genişliğini ve sonlandırma empedansını ifade eden denklemler türetilmiştir. Boyutsal parametreleri ve öngerilim voltajını belirlemek için bir tasarım yönergesi tanımlanmıştır. Önerilen birleşik

rezonatör yapısı, %5'e kadar kesirli bant genişliği sunar. 100 nm boşluk yüksekliğine sahip bir polisilikon plaka kullanılan tipik bir tasarım için, sonlandırma empedansının merkez frekansına oranı $158 \Omega/\text{MHz}$ olarak hesaplanmıştır. Bu sonuç, çip üzeri ara frekans (IF) filtrelerinin, bu tip birleştirilmiş rezonatörler kullanılarak birkaç yüz MHz'e kadar merkez frekanslarda uygulanabileceğini gösterir. Yapılan çalışmayı deneysel olarak doğrulamak için birleştirilmiş bir rezonatör tasarlanmış ve üretilmiştir. Bu birleştirilmiş rezonatörün ölçüm sonuçları, eşdeğer devre modeli simülasyonları ile iyi bir uyum göstermektedir.

Anahtar sözcükler: Devre modellemesi, kenetlenmiş dairesel plaka rezonatörü, birleştirilmiş rezonatörler, yonga üzeri IF filtre.

Acknowledgement

First and foremost, I am incredibly grateful to my supervisors, Prof. Hayrettin Köymen and Prof. Abdullah Atalar, for their invaluable guidance and patience during my PhD study. It is an exceptional honor to get exposed to their wisdom and extensive engineering perspective. Prof. Hayrettin Köymen is a great mentor for me to get through the various challenges in both academic and daily life. His continuous support and belief in me kept me motivated and allowed me to complete this thesis. I learned a lot from the brilliant vision of Prof. Abdullah Atalar. I remember the sketch he drew when he first explained the core idea of this study. I was inspired by his way of teaching and approaching problems. It was a unique privilege to carry out academic studies and technical projects under his supervision.

I would like to thank the Thesis Monitoring Committee, Prof. Vakur Behçet Ertürk, Prof. Coşkun Kocabaş and Prof. Barış Bayram for their enlightening comments and contributions. I would like to extend my sincerest thanks to the Chairman of the Thesis Defence Committee, Prof. Sencer Koç, for his time and valuable comments.

It was a pleasure to meet Dr Mehmet Yılmaz during the last two years of my studies. He helped me a lot with the clean-room activities, which led to significant findings to uncover the measurement results. I would like to express my gratitude for his support and belief in this work.

I would like to thank my friends, colleagues and research mates Ceyhun Kelleci, Akif Alperen Coşkun, Fırat Karataş, Kağan Oğuz and Elif Aydoğdu for the helpful discussions.

Finally, I am deeply indebted to my beloved wife, Sevgi, for her endless love, continuous support and understanding throughout the time required to complete this study. I am thankful to my lovely son, Çınar, for being a joy in my life and motivation to cope with the challenges.

Dedicated to my beloved wife, Sevgi, and my lovely son, ınar...

Contents

1	Introduction	1
2	Coupled-Resonator Structure	5
3	Small-Signal Equivalent Circuit Model	8
	3.1 Single Resonator Model.....	8
	3.2 Coupled-Resonator Model	12
4	Coupled-Resonator Design	18
	4.1 Defining Design Specifications	18
	4.2 Design Procedure	20
5	An Example Design	23
6	Experimental Verification	28
	6.1 Test Setup.....	28
	6.2 Measurement Results	33
7	Conclusions	38
A	ANSYS Code for the Simulation of Mechanically Coupled Clamped Circular Plate Resonators.....	44
B	The Equivalent Circuit Model Implementation in ADS	49

List of Figures

2.1	(a) Top view with geometrical details and I/O electronic circuitry and (b) unbiased A-A' cross-sectional view of the proposed mechanically coupled clamped circular plate resonators.	5
2.2	Cross-sectional views of (a) out-of-phase and (b) in-phase mode shapes of the proposed mechanically coupled clamped circular plate resonators.	6
2.3	(a) The normalized peak displacements and (b) the phases of input and output resonators as a function of normalized frequency, for $\alpha = 0.05$	7
3.1	Small-signal equivalent circuit model of a clamped circular plate resonator under vacuum (for both the medium and gap).	9
3.2	A comparison of displacement profiles for static $X(r)$ and dynamic $x(r)$ (at fundamental resonance frequency) excitations normalized to X_P and x_P , respectively.	11
3.3	Small-signal equivalent circuit model of the coupled-resonator structure. .	13
3.4	The simplified form of the small-signal equivalent circuit model of the coupled-resonator structure.	13
3.5	FEM simulation results for the electrical input impedance.	15
3.6	FEM simulation results for the spring softening capacitance.	15
3.7	FEM simulation results and polynomial fit for the CR1 parameter.	16
3.8	FEM simulation results and polynomial fit for the CR2 parameter.	17
4.1	$ S_{21} $ simulation result of example design 1 indicates 10 MHz center frequency and 490 kHz bandwidth under 10 k Ω impedance terminations. .	21
4.2	$ S_{21} $ simulation result of example design 2 indicates 107 MHz center frequency and 1 MHz bandwidth under 3.4 k Ω impedance terminations. .	22
4.3	$ S_{21} $ simulation result of example design 3 indicates 127 MHz center frequency and 5 MHz bandwidth under 17 k Ω impedance terminations. .	22

5.1	Photograph of the whole chip fabricated using the PolyMUMPs multi-project wafer service. The die site is 10 mm x 10 mm.....	24
5.2	(a) Top view SEM image and (b) the cross-section illustration (not drawn to scale) of a coupled-resonator device based on the PolyMUMPs process.....	25
5.3	SEM views of FIB-cuts showing the cross-section of (a) the moving plate anchored to the substrate and (b) the overlap region including the moving plate and the bottom electrodes.	26
6.1	Layout of the test structures for the layer resistivity evaluation.	28
6.2	Photo of a coupled-resonator unit wire-bonded to a carrier board.	30
6.3	Photo of the carrier board including the bias tees and coaxial connections.....	30
6.4	Photo of the carrier board inside a vacuum chamber.	31
6.5	Photo of a coupled-resonator unit connected to a test board through a probe station. The test setup is placed inside a vacuum chamber.	32
6.6	Photo of a coupled-resonator unit under probe station.....	33
6.7	Schematic diagram of the test board.	33
6.8	S-parameter measurement results of the device #1.	34
6.9	S-parameter measurement results of the device #2.	35
6.10	$ S_{21} $ (solid line) and $ S_{11} $ (dashed line) simulation results of the sample coupled-resonator device #3 for VDC = 16 V up to 22 V in 2 V steps (from right to left) under vacuum.....	37
6.11	Measurement results of $ S_{21} $ transmission characteristics of the sample coupled-resonator device #3 for VDC = 16 V up to 22 V in 2 V steps (from right to left) under vacuum.....	37
B.1	ADS small-signal schematic setup for the coupled-resonator filter.....	49
B.2	The half section of the coupled-resonator implemented in ADS.	50

List of Tables

2.1	Definitions of the parameters given in Fig. 2.1.....	6
3.1	Definitions of the model parameters shown in Fig. 3.1.	9
4.1	Parameters of three example designs for polysilicon plate material.	21
5.1	Material properties of the PolyMUMPs structural layers of polysilicon (Poly1 and Poly2).....	23
6.1	Design dimensions of the device #1.....	34
6.2	Design dimensions of the device #2.....	35
6.3	Measured dimensions of the device #3.	36

Chapter 1

Introduction

Mechanical filters date back to the late 1930s [1]. The mechanical filters replaced the lumped electronic filters, taking advantage of the small form factor and high-Q of mechanical resonators. The operation principle of a mechanical filter is as follows: Electrical input signals are converted to mechanical energy by a transducer. Mechanical resonators coupled via mechanical rods perform filtering in the mechanical domain. A second transducer is used to transform the filtered mechanical signals into electrical output. Magnetostrictive materials were employed to be the transducers of early designs [1–3]. Piezoelectric transducers emerged later [4–6] due to their superior conversion efficiency and reliability. Analytical derivations, circuit design methods, and application examples for common mechanical filter types were given in [7].

A new era started for mechanical filters with commercially available MEMS technology more than two decades ago. Small-scale, high-Q, micro-electromechanical resonators based on CMOS compatible processes enabled on-chip integration of MEMS filter structures with electronic circuitry [8–11].

Lin et al. [12], Wang and Nguyen [13], and Jing et al. [14] introduced mechanically coupled comb-transduced resonator filters using micromachining techniques. These resonators move laterally, and beam springs provide mechanical coupling. This type of filter is vulnerable to fabrication tolerances due to its mechanical complexity. Also, the highest center frequency achievable is in the order of 1MHz. On the other hand, Bannon et al. [15] and Motiee et al. [16] used beam coupled clamped-clamped beam resonators. Compared to the mechanically coupled comb-transduced resonators, these coupled-resonators

have relatively low mechanical complexity and offer up to ten times higher center frequencies.

Pourkamali and Ayazi [17, 18] and Galayko et al. [19] introduced non-mechanical coupling, either capacitive or electrostatic, between clamped-clamped beam resonators. There are two main advantages of the non-mechanical coupling approach: the low mechanical complexity and the post-production tuning capability of the coupling strength. However, it is essential to emphasize that the latter advantage requires the necessity to control the independent bias voltages of the resonators.

Li et al. [20, 21] and Shalaby et al. [22] reported bulk acoustic mode resonator-based filters. The bulk acoustic mode resonators exhibit higher effective stiffness than their flexural mode counterparts, making them suitable for higher frequency applications. Mechanically coupled radial-contour mode disk arrays were demonstrated to reduce the termination impedance and suppress unwanted spurious modes [20, 21].

In [12–22], the conceptual lumped element electrical circuit analogies are used to predict the performance of the resonators and filters. Equivalent circuit model parameters are arbitrarily tuned according to the measurement results. By employing these adjusted element values, the comparable performance of equivalent circuits is demonstrated. This kind of modeling approach does not help design new structures since the model elements are not represented by the correct functions of the design variables.

Greywall and Busch [23] presented mechanically coupled drumhead resonator filters. The input resonator is electrically driven using a circular ring electrode, and the displacement amplitude of the output resonator is sensed using optical interference techniques. The cyclic connections of up to 20 coupled-resonators were demonstrated, and symmetric bandpass filter response was achieved without post-production tuning.

This thesis investigates the properties of mechanically coupled clamped circular plate resonators, as explained in Chapter 2. The main focus is to have accurate modeling that enables successful and fast designs before production. To

achieve this aim, we develop a lumped element equivalent circuit model of the coupled-resonators in Chapter 3. As a beneficial outcome, we provide analytical derivations in Chapter 4, which determine the practical limits of these coupled-resonators for on-chip filter applications [24].

In the model development, we use a modified version of the small-signal equivalent circuit model of the capacitive micromachined ultrasonic transducer (CMUT) given in [25] that was developed for a single clamped circular plate resonator. Herein, we introduce two main modifications to this model: Firstly, the resonance frequency prediction of the model is updated based on the analytical solution of the equation of motion for a vibrating clamped circular plate. In addition to the static compliance parameter, the dynamic compliance parameter is proposed in this context. Secondly, change in the displacement profile due to partial electrode usage and electrostatic excitation is taken into account using a FEM-based correction factor, which scales the static compliance of the plate given in [25]. The developed single resonator model is accurate and comparable to FEM for any given set of dimensions, bias voltage, and material properties.

We develop a coupled-resonator model based on the single resonator model and the capacitive coupling approach. Model parameters of the coupled-resonators are expressed in terms of the single resonator model parameters and the amount of overlap between resonators using analytical derivations and FEM simulation results. Since we do not repeat the FEM simulations used for the model development, the model implemented in a circuit simulator allows for fast optimization of design parameters for given specifications, like center frequency, bandwidth, and optimal termination impedance.

In our coupled-resonator approach, the coupling mechanism does not require any additional mechanical element similar to the structure used in [23], unlike the commonly used coupled MEMS resonator structures. Instead, the clamped circular plate resonators are deliberately overlapped to form the mechanical coupling generated at the interface. Compared to the coupled-resonators with a separate mechanical coupling element, the mechanical complexity is reduced,

and the reliability is increased. The resulting structure differs from the one given in [23], considering the shape of the electrodes and the type of output. We prefer to use whole circular electrodes, rather than the ring-shaped electrodes used in [23], to achieve higher excitation efficiency of the fundamental mode resonance and a higher electromechanical transformation ratio, which reduces the termination impedance value. In order to allow proper integration with electronic circuitry, electrical output is implemented instead of the optical interference technique-based output detection method described in [23]. Furthermore, no modeling work occurs in [23] while we propose an experimentally validated equivalent circuit model.

The spatial velocity of the vibrating clamped circular resonator plate decreases as the radial location becomes distant from the central point and goes to zero at the clamped periphery. The proposed structure inherently provides low-velocity coupling [26] between the resonators without the need for a mechanical coupling element. The low-velocity coupling methodology allows us to achieve narrower filter bandwidths compared to coupling the resonators at their maximum velocity points.

In Chapter 5, the implementation of a coupled-resonator design based on a commercial process is presented. Although the gap height and resonator thickness options provided in this process limit the lowest termination impedance, this process is used to demonstrate the validity of our model. Measurement results are in good agreement with our model predictions, as explained in Chapter 6. Finally, Chapter 7 summarizes the work done in this thesis.

Chapter 2

Coupled-Resonator Structure

We propose a new coupled micromechanical resonator structure. The clamped circular plate is selected as the resonator unit. Two resonator plates are overlapped, i.e., overlap ratio (α) defined in Fig. 2.1 is between 0 and 0.1. The clamps of each resonator at the overlapped region are removed to form the coupling mechanism. In other words, the resonator plates are mechanically connected and free to move at the overlapping region. Graphical representation and the dimensional parameters of mechanically coupled clamped circular plate resonators are given in Fig. 2.1. Definitions of the parameters are listed in Table 2.1. We express the effective gap height as $t_{ge} = t_g + t_i/\epsilon_r$, where ϵ_r is the relative permittivity of the insulating material. Analytical expression of a

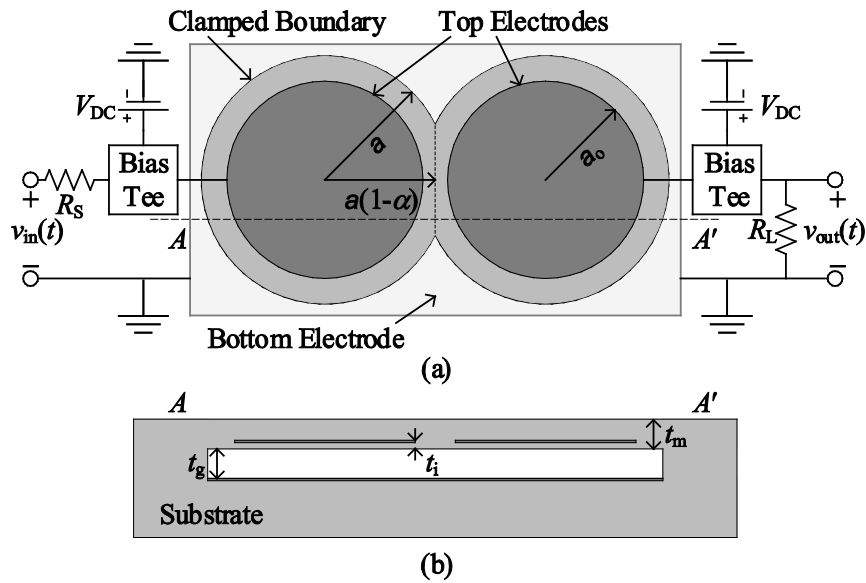


Figure 2.1: (a) Top view with geometrical details and I/O electronic circuitry and (b) unbiased A-A' cross-sectional view of the proposed mechanically coupled clamped circular plate resonators.

practical parameter called overlap area ratio (Δ), i.e., the overlap area divided by the original circular resonator area, is

$$\Delta = \frac{1}{\pi} \left(\cos^{-1}(1-\alpha) - (1-\alpha) \sin(\cos^{-1}(1-\alpha)) \right). \quad (2.1)$$

a :	The radius of the resonator plates
a_0 :	The radius of the top electrodes
t_m :	The thickness of the resonator plates
t_g :	The gap height
t_i :	The insulator thickness below the top electrodes
R_S/R :	The source/load termination resistance
α :	The overlap ratio

Table 2.1: Definitions of the parameters given in Fig. 2.1.

The operation principle of the coupled-resonators is as follows: An electrical signal is applied between the input resonator plate and the bottom electrode. The resulting electrostatic forces vibrate the input resonator plate. Then, the generated mechanical energy is transferred to the output resonator plate through the mechanical coupling interface and converted back to an electrical signal between the output resonator plate and the bottom electrode. The overall electrical signal transfer process is frequency selective since the coupled-resonator structure has two fundamental resonances. Cross-sectional views of these resonance mode shapes are illustrated in Fig. 2.2. The lower frequency

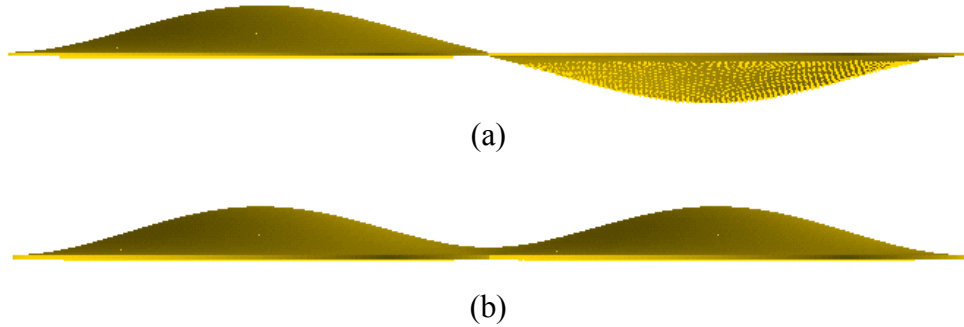


Figure 2.2: Cross-sectional views of (a) out-of-phase and (b) in-phase mode shapes of the proposed mechanically coupled clamped circular plate resonators.

resonance corresponds to the out-of-phase movement of the resonators. On the other hand, the higher frequency resonance happens when the resonators are moving in phase. Normalized peak displacements and phases of the input and output resonators as functions of frequency are plotted in Fig. 2.3. The frequency axis is normalized with the fundamental resonance frequency of a

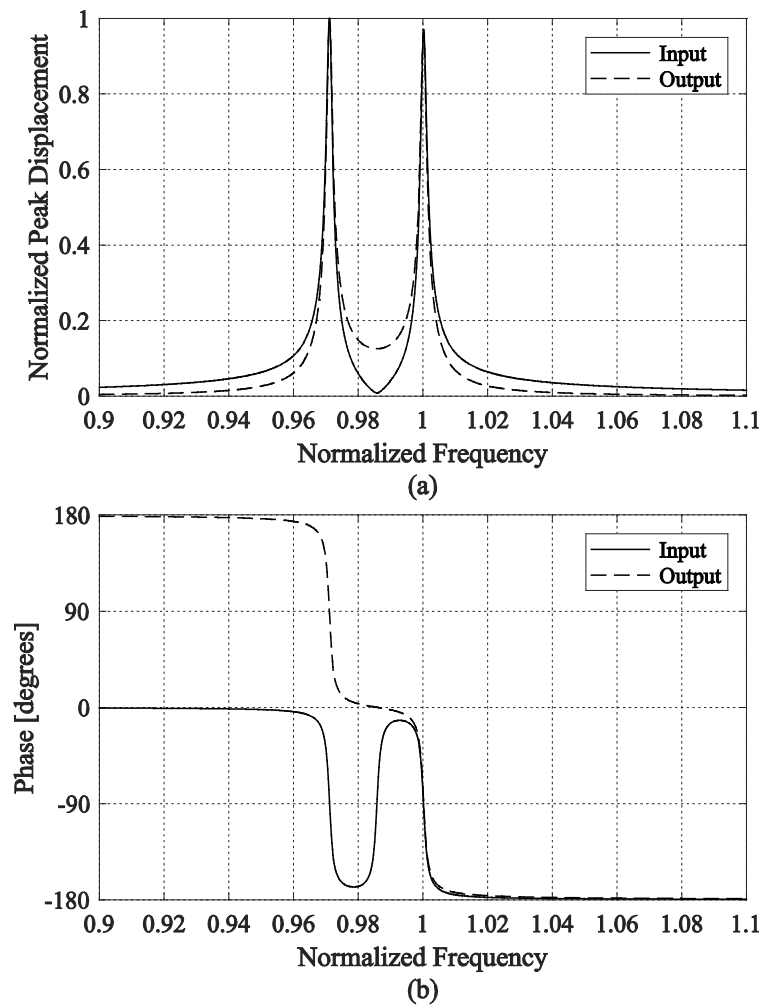


Figure 2.3: (a) The normalized peak displacements and (b) the phases of input and output resonators as a function of normalized frequency, for $\alpha=0.05$.

single and fully clamped circular plate resonator, a reference resonator. There is an anti-resonance behavior in between the two resonance frequencies. The input resonator stays stationary at this specific frequency while the output resonator moves in phase with the input signal.

Chapter 3

Small-Signal Equivalent Circuit Model

We introduce a small-signal equivalent circuit model for mechanically coupled clamped circular plate resonators, valid for the overlap ratio range $0 < \alpha < 0.1$. Altering the overlap ratio adjusts the coupling coefficient between the two resonators and determines the fractional bandwidth up to 5%. We define each model parameter as a function of the corresponding single resonator model parameter and the overlap ratio.

3.1 Single Resonator Model

The small-signal equivalent circuit model of a single clamped circular plate resonator is given in [25]. Since we develop our coupled-resonator model based on a modified version of the model in [25], we review and summarize the model parameters in this section. The small-signal equivalent circuit model of a single clamped circular plate resonator under vacuum (for both the medium and gap) is shown in Fig. 3.1. The model parameters are defined in Table 3.1, and can be expressed as

$$C_{0d} = C_0 g \left(\frac{X_P}{t_{ge}} \right), \quad (3.1)$$

$$n_R = \sqrt{5} \frac{C_0 V_{DC}}{t_{ge}} g' \left(\frac{X_P}{t_{ge}} \right), \quad (3.2)$$

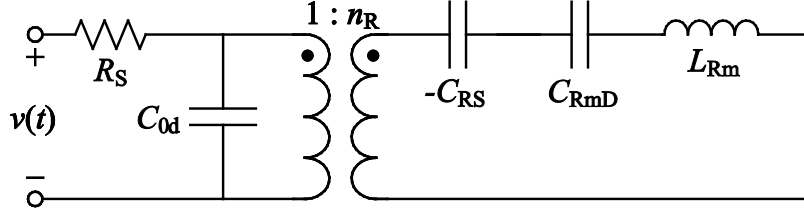


Figure 3.1: Small-signal equivalent circuit model of a clamped circular plate resonator under vacuum (for both the medium and gap).

C_{0d} :	The electrical input capacitance
n_R :	The rms electromechanical turns ratio
C_{RS} :	The rms spring softening capacitance
L_{Rm} :	The rms mass
C_{RmD} :	The rms dynamic compliance

Table 3.1: Definitions of the model parameters shown in Fig. 3.1.

$$C_{RS} = \frac{2t_{ge}^2}{5C_0V_{DC}^2g''(X_P/t_{ge})}, \quad (3.3)$$

$$L_{Rm} = \rho\pi a^2 t_m, \quad (3.4)$$

and

$$C_{RmD} = 0.115 \left[\frac{(1-\sigma^2)a^2}{\pi Y_0 t_m^3} \right], \quad (3.5)$$

where

$$C_0 = \frac{\epsilon_0 \pi a^2}{t_{ge}}, \quad (3.6)$$

$$g(u) = \frac{\tanh^{-1}(\sqrt{u}) - \tanh^{-1}((1-a_0^2/a^2)\sqrt{u})}{\sqrt{u}}, \quad (3.7)$$

$$g'(u) = \frac{1}{2u} \left(\frac{1}{1-u} - \frac{1-a_0^2/a^2}{1-(1-a_0^2/a^2)^2 u} - g(u) \right), \quad (3.8)$$

$$g''(u) = \frac{1}{2u} \left(\frac{1}{(1-u)^2} - \frac{(1-a_0^2/a^2)^3}{(1-(1-a_0^2/a^2)^2 u)^2} - 3g'(u) \right), \quad (3.9)$$

ε_0 is the permittivity of free space, X_p is the peak static displacement under VDC bias voltage, Y_0 is Young's modulus, σ is Poisson's ratio, and ρ is the mass density of the plate.

The X_p parameter can be determined using the static force equilibrium under uniform force distribution assumption, which yields

$$\frac{V_{DC}}{V_r} = \sqrt{\frac{3 \left(\frac{X_p}{t_{ge}} \right)}{2g' \left(\frac{X_p}{t_{ge}} \right)}}, \quad (3.10)$$

where

$$V_r = \sqrt{\frac{4t_{ge}^2}{15C_{RMS}C_0}} \quad (3.11)$$

and

$$C_{RMS} = \frac{9}{80} \left[\frac{(1-\sigma^2)a^2}{\pi Y_0 t_m^3} \right], \quad (3.12)$$

which is the rms static compliance of the clamped circular plate [25].

C_{RmD} is a contribution of this work into the existing model. C_{RmD} is approximately 2.2% higher than C_{RmS} , which is calculated under uniform static force distribution assumption and results in a static displacement profile [27–29] given as

$$X(r) = X_p \left(1 - \left(\frac{r}{a} \right)^2 \right)^2 \quad \text{for } r \leq a. \quad (3.13)$$

On the other hand, C_{RmD} is determined by the fundamental resonance frequency for a clamped circular plate obtained using plate theory [30, 31], as

$$f_0 = \frac{1}{2\pi\sqrt{L_{Rm}C_{RmD}}} = 0.469 \frac{t_m}{a^2} \sqrt{\frac{Y_0}{(1-\sigma^2)\rho}}. \quad (3.14)$$

The dynamic displacement profile at the fundamental resonance frequency derived based on the solution of the classical differential equation of motion [30, 31] is given by

$$x(r,t) \approx x_p(t) \left(\frac{J_0\left(3.20\frac{r}{a}\right) - \frac{J_0(3.20)}{I_0(3.20)} I_0\left(3.20\frac{r}{a}\right)}{1 - \frac{J_0(3.20)}{I_0(3.20)}} \right) \text{ for } r \leq a, \quad (3.15)$$

where x_p is the dynamic peak displacement at f_0 , J_0 is the order 0 Bessel function of the first kind, and I_0 is the order 0 modified Bessel function of the first kind.

Normalized static and dynamic displacement profiles are plotted in Fig. 3.2. Ratios of peak to rms displacement are $X_p/X_R = \sqrt{5}$ and $x_p/x_R = \sqrt{5.47}$ for static and dynamic responses, respectively. Since the difference between these two profiles is not significant, we derive the model parameters assuming the static displacement profile is also valid in the vicinity of the fundamental resonance frequency.

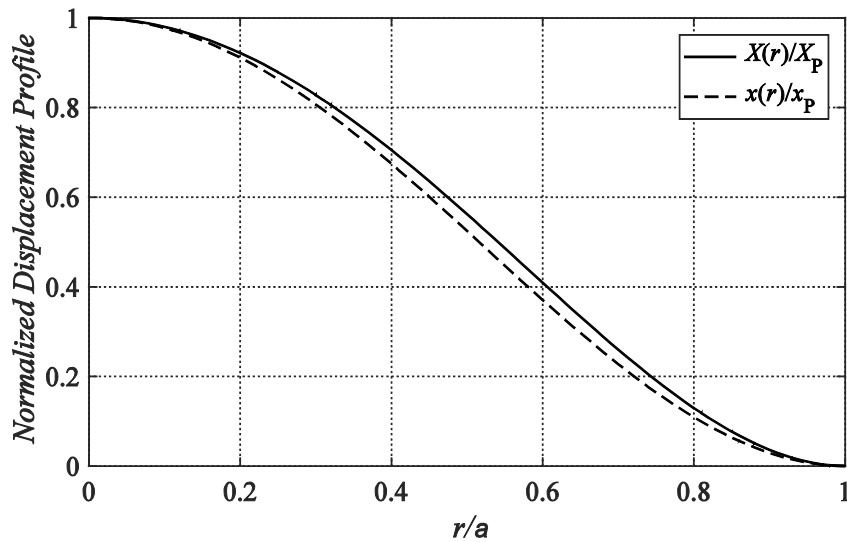


Figure 3.2: A comparison of displacement profiles for static $X(r)$ and dynamic $x(r)$ (at fundamental resonance frequency) excitations normalized to X_p and x_p , respectively.

Due to the partial electrode usage and electrostatic force distribution, which is inversely proportional to the square of the $t_{ge}-X(r)$, the actual force distribution becomes more concentrated at the center of the circular plate concerning the uniform force distribution case. Consequently, the solution of X_p using (3.10), (3.11), and (3.12) underestimates the correct result. We can achieve more accurate model parameters by introducing the effective rms static compliance of the resonator plate as

$$C_{\text{RmSe}} = \beta C_{\text{RmS}} \quad \text{for } \beta > 1, \quad (3.16)$$

where β is the correction factor for compensating the non-uniform force distribution. As a result, using (3.11) and (3.16), the effective V_r parameter becomes

$$V_{\text{re}} = \frac{V_r}{\sqrt{\beta}}. \quad (3.17)$$

For the partial electrode radius $\mathbf{a}_o = 0.8\mathbf{a}$, we found that β equals 1.028 based on fitting the model outcome with the FEM simulation results. We do not determine the exact displacement profile with this approach. Instead, we use the effective rms static compliance to compensate for the changes in the model parameters due to the deviation from the displacement profile given in (3.13).

3.2 Coupled-Resonator Model

The equivalent circuit model of each coupled-resonator is defined as an element-wise updated version of the model given in Fig. 3.1 for a single clamped circular plate resonator. The primary coupling mechanism between the resonators is mechanical. Electromagnetic coupling between the electrodes is also verified to be negligible based on electromagnetic simulations. The mechanical coupling between the resonators can be represented with a shunt capacitance C_{RC} between the equivalent circuit models of the resonators. Since the rms velocity of resonator plates and overlapping boundary are related to each other with a constant ratio, a transformer with a turns ratio of

$$n_{RC} = \sqrt{\frac{k_{RC}}{k_R}} \quad (3.18)$$

is placed at the coupling port of each resonator's equivalent circuit model, where k_{RC} is the rms stiffness at the overlapping boundary, and k_R is the overall rms stiffness of the resonator plate [13]. The small-signal equivalent circuit model of the coupled-resonator structure is given in Fig. 3.3. C_{R1} is the compliance of each resonator coupled. In order to simplify the model given in Fig. 3.3, we can

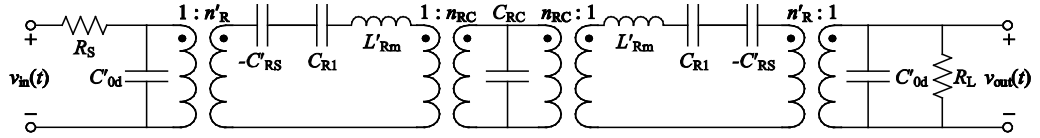


Figure 3.3: Small-signal equivalent circuit model of the coupled-resonator structure.

replace the C_{RC} and neighboring transformers with two parallel capacitances evaluated as

$$C_{R2} = \frac{n_{RC}^2 C_{RC}}{2}. \quad (3.19)$$

The resulting small-signal equivalent circuit model is depicted in Fig. 3.4.

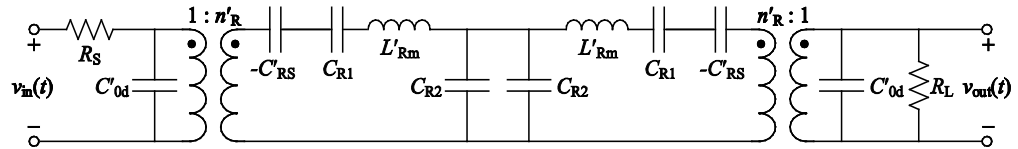


Figure 3.4: The simplified form of the small-signal equivalent circuit model of the coupled-resonator structure.

It is helpful to address the fundamental resonance modes to have a better understanding of this model. At lower frequency resonance, the velocity vectors of the resonators are out of phase ($v_{r2} = -v_{r1}$) so that velocity at the coupling region (v_{rC}) is zero and the coupling node becomes a virtual ground. The

resulting resonance frequency is governed by C_{R1} compliance. At higher frequency resonance, the velocity vectors of the resonators are in phase ($v_{r2}=v_{r1}$). In this case, v_{rC} is nonzero, and the coupling capacitor has a loading effect at each resonator. The resulting resonance frequency is governed by the series combination of C_{R1} and C_{R2} . Since the overall compliance is reduced, this mode corresponds to a higher frequency.

The mass of each resonator plate is modified due to the resonator area reduction as

$$L'_{Rm} = L_{Rm}(1-\Delta). \quad (3.20)$$

Based on the FEM simulations and relative to the single resonator model parameters given in (3.1), (3.2), and (3.3), extracted small-signal equivalent circuit model parameters of the electrical input capacitance, rms electromechanical turns ratio, and rms spring softening capacitance turned out to be

$$C'_{0d} \approx C_{0d}, \quad (3.21)$$

$$n'_R \approx n_R \sqrt{(1-\Delta)}, \quad (3.22)$$

and

$$C'_{RS} \approx \frac{C_{RS}}{(1-\Delta)}, \quad (3.23)$$

respectively, having less than 0.5% error for the overlap ratio range $0 < \alpha < 0.1$ and $V_{DC}/V_{re} \leq 0.9$. Fig. 3.5 and Fig. 3.6 show the related FEM extracted data for various bias voltage and overlap ratio values.

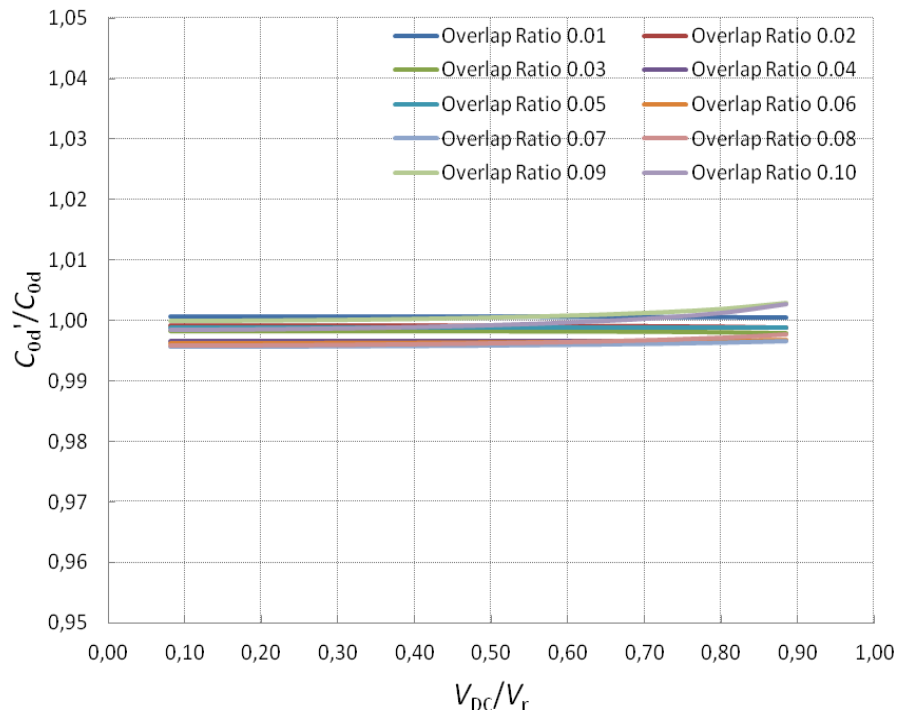


Figure 3.5: FEM simulation results for the electrical input impedance.

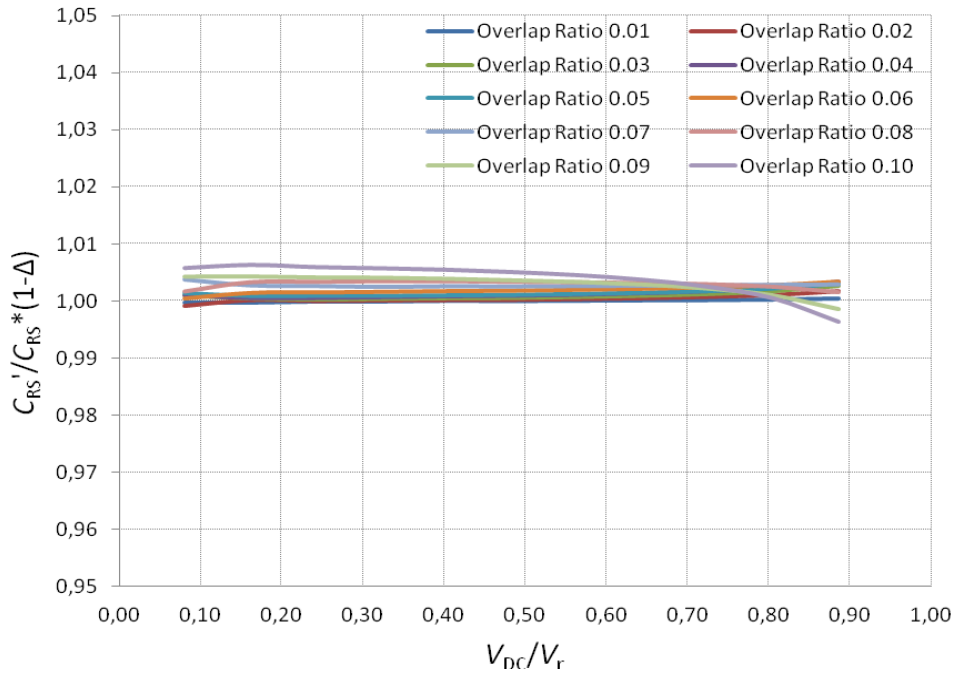


Figure 3.6: FEM simulation results for the spring softening capacitance.

Mechanical compliance parameters C_{R1} and C_{R2} can be approximated by 3rd order polynomial fit to the FEM simulation results for the overlap ratio range $0 < \alpha < 0.1$ as

$$C_{R1} \approx \frac{C_{RmD}(1-\Delta)}{1-1.20\alpha-0.305\alpha^2+14.5\alpha^3} \quad (3.24)$$

and

$$C_{R2} \approx \frac{C_{RmD}(1-\Delta)}{\alpha(1.19-4.01\alpha-27.5\alpha^2)}, \quad (3.25)$$

respectively. Corresponding FEM simulated data are given in Fig. 3.7 and Fig. 3.8.

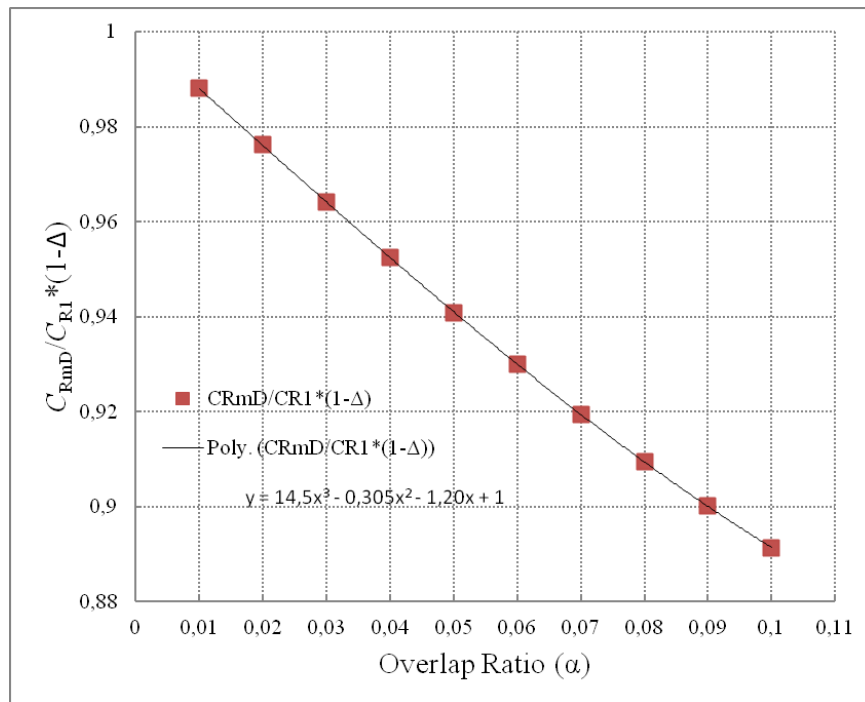


Figure 3.7: FEM simulation results and polynomial fit for the C_{R1} parameter.

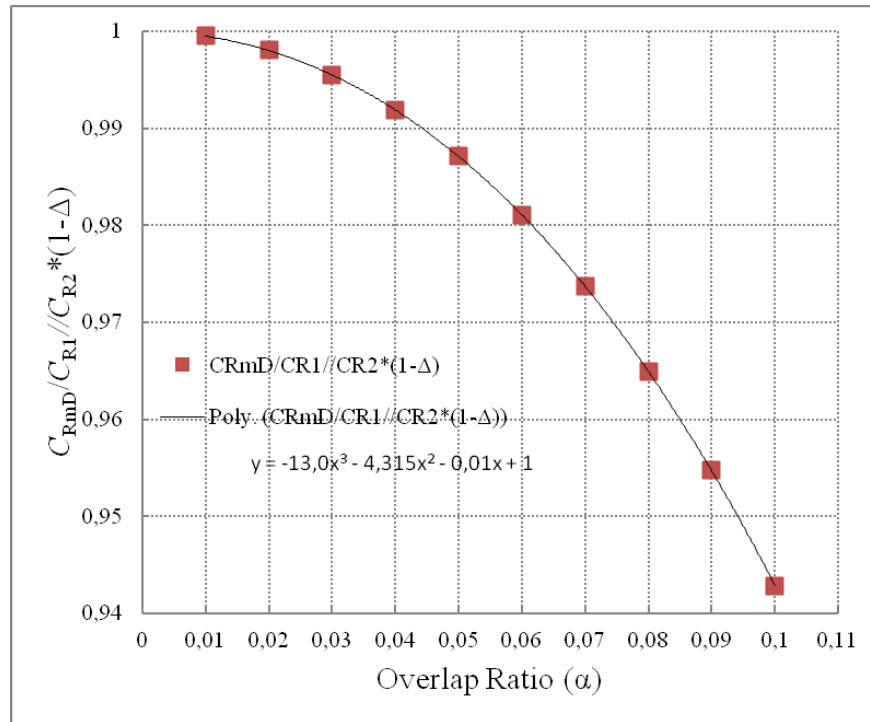


Figure 3.8: FEM simulation results and polynomial fit for the C_{R2} parameter.

As the overlap ratio (α) goes to 0, the coupling between the resonators becomes negligible. Thus, the coupled-resonator model in Fig. 3.4 approaches the model of two uncoupled resonators, one of which is shown in Fig. 3.1.

We have derived all of the model parameters based on the analytical derivations and the FEM simulation results. The small-signal equivalent circuit model given in Fig. 3.4 is implemented in ADS¹ circuit simulator and verified for several dimensional parameters by comparing the circuit simulator results with the FEM simulation results.

¹PathWave Advanced Design System, Keysight Technologies, Inc., Santa Rosa, CA, USA.

Chapter 4

Coupled-Resonator Design

4.1 Defining Design Specifications

We have a complete small-signal equivalent circuit model for mechanically coupled clamped circular plate resonators. It is helpful to have an analytical derivation of the dimensional parameters for setting the initial values before the optimization routine. We need to control center frequency, bandwidth, and termination impedance for a specific bandpass filter design.

Based on the frequency and phase responses given in Fig. 2.3 and the model shown in Fig. 3.4, the out-of-phase and the in-phase resonance frequencies of the coupled-resonator structure can be expressed as:

$$f_1 = \frac{1}{2\pi} \sqrt{\frac{1}{L'_{Rm}} \left(\frac{1}{C_{R1}} - \frac{1}{C'_{RS}} \right)} \quad (4.1)$$

and

$$f_2 = \frac{1}{2\pi} \sqrt{\frac{1}{L'_{Rm}} \left(\frac{1}{C_{R1}} + \frac{1}{C_{R2}} - \frac{1}{C'_{RS}} \right)}, \quad (4.2)$$

respectively.

We define the center frequency as $f_c = 0.5(f_1 + f_2)$, which shifts down as the overlap ratio and DC bias voltage increase. The bandwidth is assumed to be the frequency difference between in-phase and out-of-phase resonance modes, i.e., $B = f_2 - f_1$. Unlike the center frequency, the bandwidth increases as the DC bias increases. The bias voltage of the resonators is set to $V_{DC} = 0.9V_{re}$, considering the

trade-off between termination impedance and linearity. We can approximate the center frequency and the bandwidth for the overlap ratio range $0 < \alpha < 0.1$ under $\mathbf{a}_0 = 0.8\mathbf{a}$ and $V_{DC}/V_{re} = 0.9$ conditions as

$$f_c \approx f_0(0.784 - 0.333\alpha + 0.812\alpha^2 - 6.39\alpha^3) \quad (4.3)$$

and

$$B \approx f_c \alpha (0.953 - 1.70\alpha - 31.3\alpha^2), \quad (4.4)$$

respectively. The fractional bandwidth, B/f_c , reaches its maximum value of $\sim 5\%$ at $\alpha \approx 0.084$, which is in the valid range of our model given for $0 < \alpha < 0.1$.

Mechanical resonator structures suffer from their high electrical input impedance characteristics. Several studies were reported on reducing the input impedance [15, 20, 21, 32–39]. We derived a closed-form analytical expression of the electrical termination impedance (Z_0) to clarify its relation to the design parameters. Initially, we ignored the effect of electrical input capacitance to simplify the calculations. Then, we compared the resulting termination impedance with the impedance of electrical input capacitance to validate this assumption. Referring to Fig. 3.4, the termination impedance, Z_0 , is obtained under the $R_S = R_L = Z_0$ condition as

$$Z_0 = \frac{2\pi L'_{Rm}}{n'_R{}^2} \frac{\sqrt{(f_c^2 - f_1^2)(f_2^2 - f_c^2)}}{f_c}. \quad (4.5)$$

We can approximate Z_0 using (4.5), (3.20), (3.22), and narrowband filter assumption, i.e., $B/f_c \ll 1$, as

$$Z_0 \approx \frac{2\pi L_{Rm} B}{n_R^2}. \quad (4.6)$$

For an electrode radius $\mathbf{a}_0 = 0.8\mathbf{a}$, we can rearrange (4.6) using (3.2), (3.4), (3.6), (3.10), (3.11), (3.12), (3.14), and (3.17) as either

$$Z_0 \approx \frac{0.116}{\varepsilon_0(X_p/t_{ge})g'(X_p/t_{ge})} \frac{\rho(1-\sigma^2)}{Y_0} \left(\frac{\mathbf{a}}{t_m}\right)^2 t_{ge} B \quad (4.7)$$

or

$$Z_0 \approx \frac{0.0543}{\varepsilon_0 \left(X_p/t_{ge} \right) g' \left(X_p/t_{ge} \right)} \sqrt{\frac{\rho(1-\sigma^2)}{Y_0}} \frac{t_{ge}}{t_m} \frac{B}{f_0}. \quad (4.8)$$

Under $a_0=0.8a$ and $V_{DC}/V_{re}=0.9$ conditions, we have $(X_p/t_{ge})=0.241$ and $g'(X_p/t_{ge})=0.447$. For the specific case of $t_{ge}=100\text{nm}$, $a/t_m=10$, $\alpha=0.01$, and the polysilicon resonator plate, the ratio of the termination impedance to the center frequency, Z_0/f_c , becomes $158 \Omega/\text{MHz}$.

The ratio of Z_0 to the impedance of the electrical input capacitance at f_c is derived using (3.1), (3.6), (3.21), and (4.7) as

$$Z_0(2\pi f_c C_{0d}) \approx 2 \left(\frac{B}{f_c} \right). \quad (4.9)$$

Since $B/f_c \ll 1$, neglecting the effect of C_{0d} is justified.

4.2 Design Procedure

To design a second-order bandpass filter with center frequency, f_c , and bandwidth, B , with a given termination impedances of Z_0 , the design procedure is as follows:

- 1) Set $a_0=0.8a$ to avoid the short circuit between the electrodes for the overlap ratio range $0 < \alpha < 0.1$.
- 2) Set $V_{DC}/V_{re}=0.9$ to achieve the lowest practical termination impedance.
- 3) Set $a/t_m=10$ to achieve as low a termination impedance as possible considering the model validity.
- 4) Find the overlap ratio α using (4.4).
- 5) Determine a and t_m using $a/t_m=10$, (3.14), (4.3), and material properties of the resonator plate.
- 6) Calculate t_{ge} using (4.7), B , and material properties of the resonator plate.
- 7) Find V_{DC} using (3.11), (3.17), and $V_{DC}/V_{re}=0.9$.
- 8) Fine-tune the parameters to achieve the desired response using the circuit simulator, ensuring that $a/t_m \geq 10$.

Table 4.1 lists the parameters of three example designs on polysilicon material. These examples show that the proposed structure is a promising candidate for small-scale on-chip IF filter applications. Having reasonable termination impedance, commonly used IF filter frequencies in the sub-GHz regime can be achieved using commercially available processes providing a gap height of 20 nm. Simulated transmission responses of the designs listed in Table 4.1 is shown in Fig. 4.1, Fig. 4.2, and Fig. 4.3.

Parameters	Design 1	Design 2	Design 3
f_c	10 MHz	107 MHz	127 MHz
B	490 kHz	1 MHz	5 MHz
Z_0	10 k Ω	3.4 k Ω	17 k Ω
t_{ge}	100 nm	20 nm	20 nm
a	27.5 μm	2.9 μm	2.4 μm
t_m	2.5 μm	290 nm	240 nm
α	0.075	0.01	0.05
V_{DC}	31 V	10 V	11 V

Table 4.1: Parameters of three example designs for polysilicon plate material.

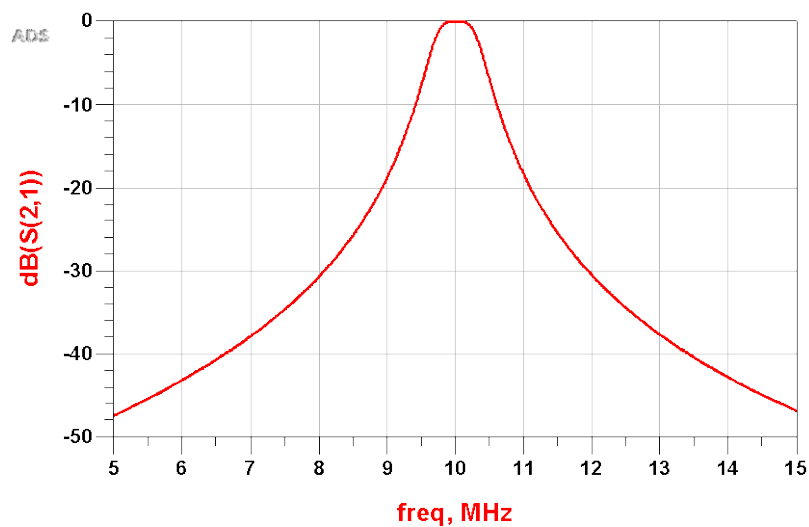


Figure 4.1: $|S_{21}|$ simulation result of example design 1 indicates 10 MHz center frequency and 490 kHz bandwidth under 10 k Ω impedance terminations.

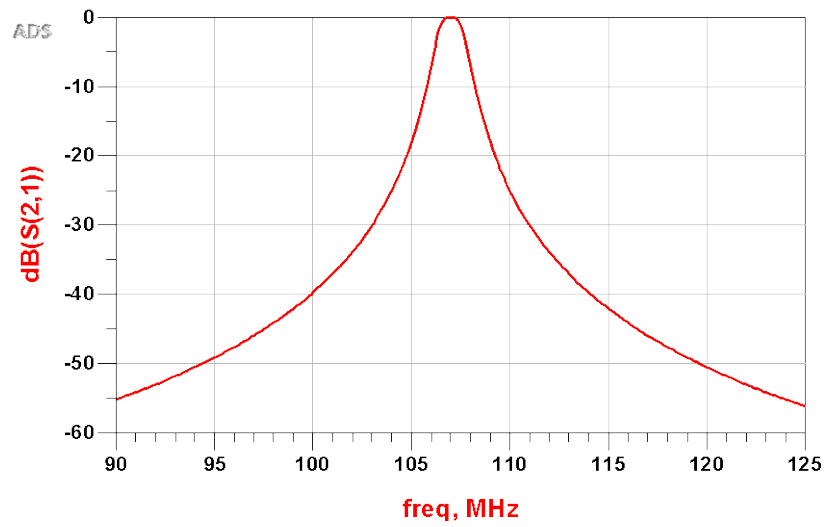


Figure 4.2 $|S_{21}|$ simulation result of example design 2 indicates 107 MHz center frequency and 1 MHz bandwidth under 3.4 k Ω impedance terminations.

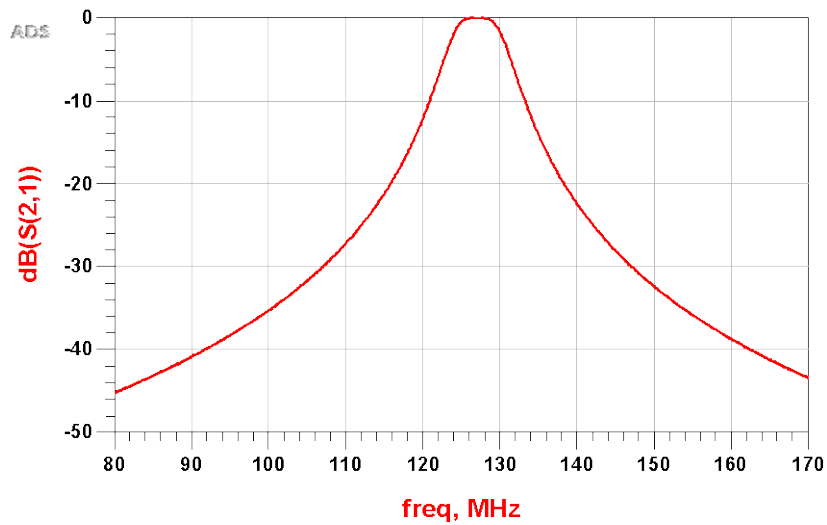


Figure 4.3 $|S_{21}|$ simulation result of example design 3 indicates 127 MHz center frequency and 5 MHz bandwidth under 17 k Ω impedance terminations.

Chapter 5

An Example Design

We used the PolyMUMPs process of MEMSCAP² and designed a coupled-resonator unit for a proof of concept demonstration. PolyMUMPs is a 3-layer polysilicon surface micromachining and bulk micromachining process. It has two sacrificial layers and one metal layer. This process is based on a silicon substrate and has a minimum feature size of 2 μm . A 600 nm thick silicon nitride layer is deposited on the substrate to provide electrical isolation between the polysilicon layers and the substrate. The first polysilicon layer, Poly0, is 500 nm thick and takes place on top of the nitride layer. Then, a 2 μm phosphosilicate glass (PSG) sacrificial layer (Oxide1) deposition follows the photolithography patterning of the Poly0 layer. The structural layers of polysilicon (Poly1 and Poly2) are 2 μm and 1.5 μm thick, respectively. Table 5.1 lists the material properties of the structural layers. In between the two structural layers, a 750 nm PSG sacrificial layer (Oxide2) is deposited. (This sacrificial layer thickness forms the gap height, t_g , of the resonator structure.) The final layer is 0.5 μm gold, which provides an electrical interface for probing and bonding. The standard die site of the PolyMUMPs multi-project wafer service is 10 mm times 10 mm.

Young's modulus, Y_0	158 \pm 10 GPa
Density, ρ	2330 kg/m ³
Poisson ratio, σ	0.22 \pm 0.01

Table 5.1: Material properties of the PolyMUMPs structural layers of polysilicon (Poly1 and Poly2).

² MEMSCAP, S.A., Cedex, France, www.memscap.com

The coupled-resonator structure introduced in Section 2 is implemented using the PolyMUMPs process for several dimensional parameter variations. The photograph of the overall chip is given in Fig. 5.1. Due to the process related measurement challenges, we could not investigate all of the design variations on the chip. However, we managed to get meaningful data from a limited number of devices. Thus, a proof-of-concept demonstration could be achieved.

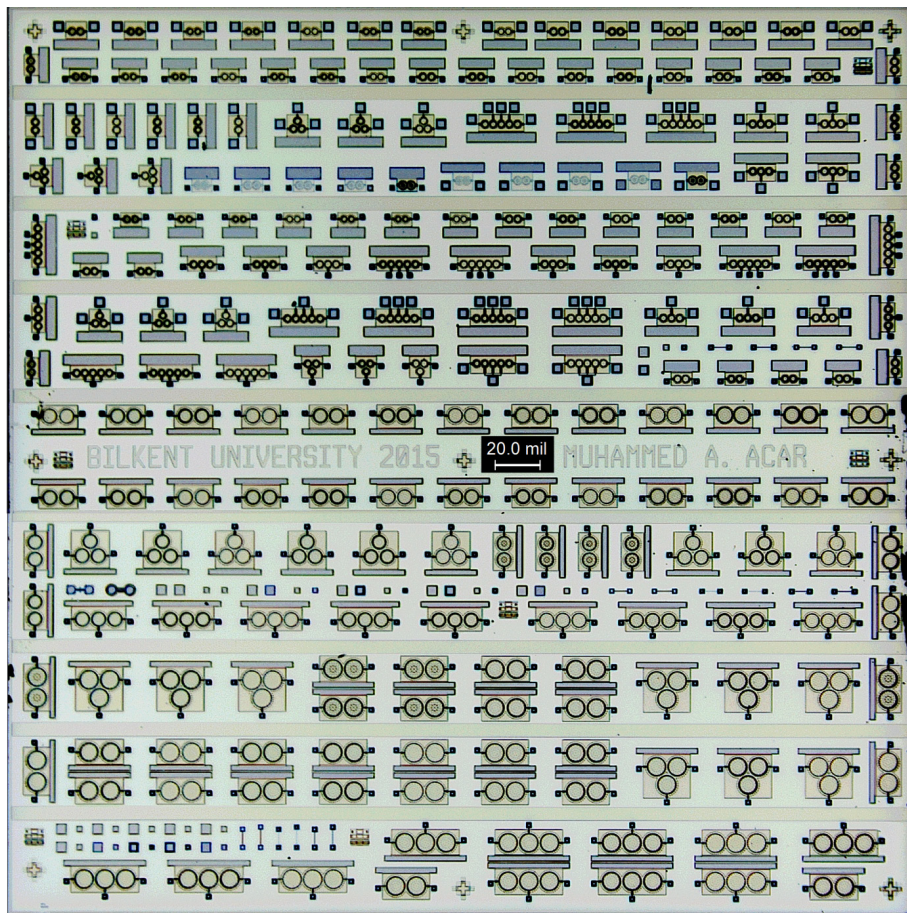
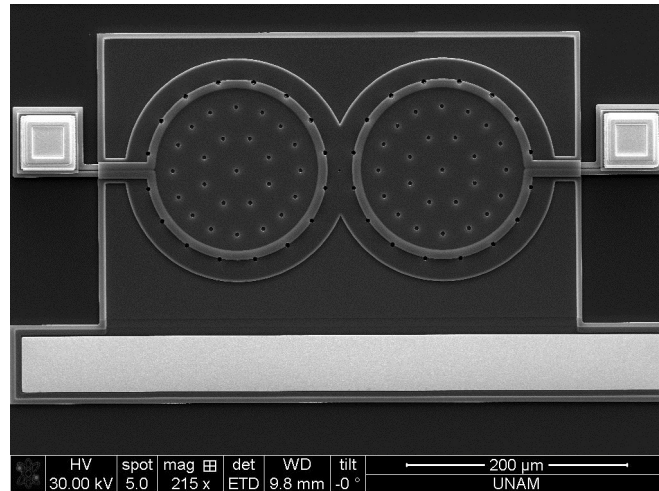


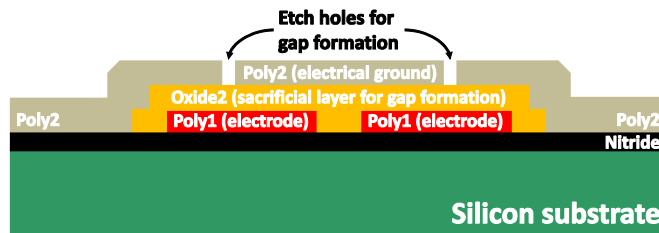
Figure 5.1: Photograph of the whole chip fabricated using the PolyMUMPs multi-project wafer service. The die site is 10 mm x 10 mm.

A top view SEM image and the cross-section illustration of a sample coupled-resonator structure are shown in Fig. 5.2. We use the Oxide2 layer for gap formation of the resonators since it provides the lowest possible gap height of 750 nm. Since the PolyMUMPs process has conductive structural layers, we cannot have isolated electrodes on mechanically coupled-resonator plates.

Instead, as shown in Fig. 5.2(b), we form the isolated electrodes using the bottom layer (Poly1) on the substrate and connect the moving plate layer (Poly2) to the electrical ground. The resulting structure in Fig. 5.2(b) is functionally



(a)

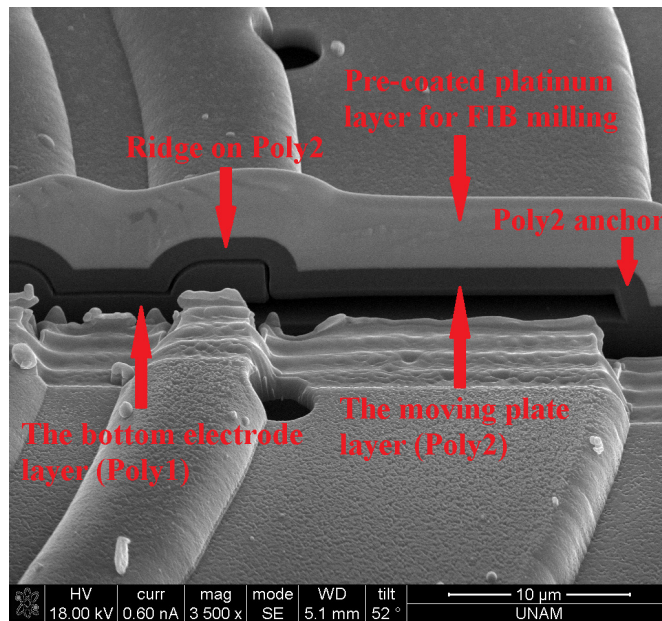


(b)

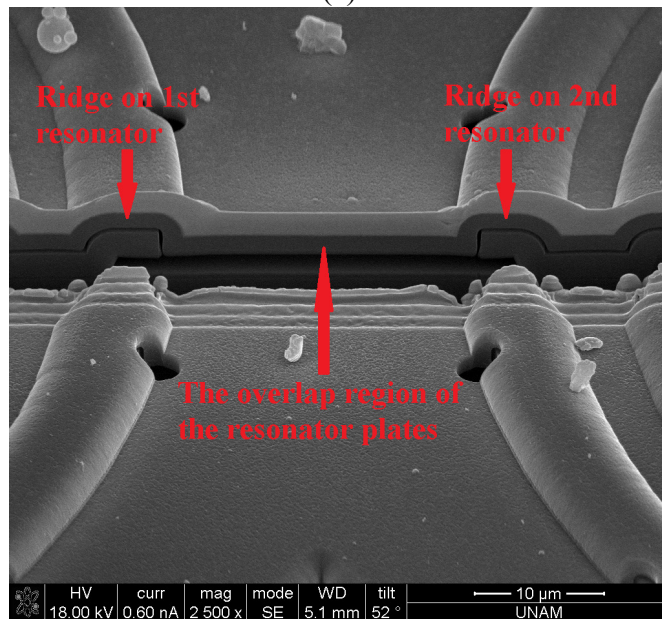
Figure 5.2: (a) Top view SEM image and (b) the cross-section illustration (not drawn to scale) of a coupled-resonator device based on the PolyMUMPs process.

equivalent to the original proposal shown in Fig. 2.1. The coupled-resonator design does not include the Poly0 and Oxide1 layers and starts with the Poly1 layer, which is used for input and output electrodes on top of the nitride isolation layer. Then, the Oxide2 layer is placed where we require the gap. We have the Poly2 layer on top as the resonator plate material. As shown in Fig. 5.2(a), this Poly2 layer has holes with a 2 μm radius and 30 μm intervals. These holes serve the removal of the sacrificial layer during the HF release process. The metal layer is used for wire bonding the input, output, and ground interconnection pads.

Although the coupled-resonator unit explained in this section is valid for the proof of concept demonstration, some structural properties of the PolyMUMPs process are different from the model assumptions. We need to take these into account when comparing the model performance with the measurements. First, the Poly2 layer is not strictly clamped at the resonator periphery. Instead, as shown in Fig. 5.3(a), it is anchored to the substrate through the stack-up of



(a)



(b)

Figure 5.3: SEM views of FIB-cuts showing the cross-section of (a) the moving plate anchored to the substrate and (b) the overlap region including the moving plate and the bottom electrodes.

Oxide1 and Oxide2 layers. The second difference is due to the conformal layer deposition of the PolyMUMPs process, i.e., every layer follows the shape underneath. Therefore, the moving plate layer is not flat as opposed to the model assumption. The circular ridges shown in Fig. 5.3 affect the elastic behavior of the moving plate. This effect is not modelled in the equivalent circuit. Fig. 5.3(b) shows the resonators' overlap region and the shape of the Poly2 layer on top of the gap. The vertical interface at the intersection of the top and the bottom electrodes produces a radial in-plane electrostatic force which is not covered in the model. Also, the sacrificial layer release holes are not present in the equivalent circuit.

Chapter 6

Experimental Verification

6.1 Test Setup

Fabricated coupled-resonator devices are first subjected to DC bias tests utilizing the probe station before the network analyzer measurements under vacuum. We apply a DC bias at the input and output electrodes through a series 1 M Ω resistor up to 90% of the expected collapse voltage. Since there is no isolation layer between the Poly2 and Poly1 layers, collapsing the plate causes electrical short and should be avoided. This test verifies the structural integrity of a device and eliminates the defective devices from further testing. Furthermore, the design has some test structures, as shown in Fig. 6.1, for evaluating the resistivity values of each polysilicon layer. The resistivity values are measured as 35 Ω /sq, 8 Ω /sq, and 22 Ω /sq for the Poly0, Poly1, and Poly2

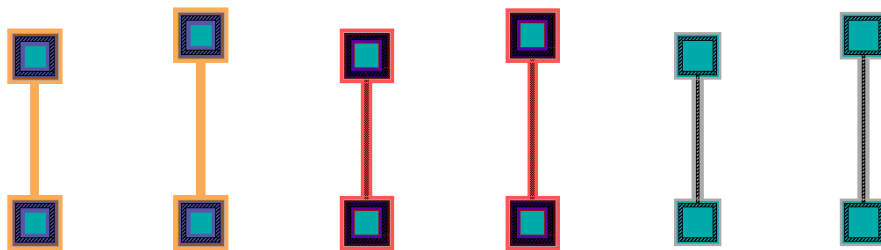


Figure 6.1: Layout of the test structures for the layer resistivity evaluation.

layers, respectively. These results are in the acceptance range provided by the foundry. The resistivity is calculated by the subtraction of the line resistances for a controlled difference in length. The parasitic resistances due to the measurement setup can be eliminated with this method.

We applied several measurement approaches throughout the characterization process of the devices. We identified the problems causing unexpected results at each step and proposed a new method to overcome the challenges until we achieved successful measurement results.

There were two main problems regarding the measurements of our devices fabricated on the PolyMUMPs process. The first one was related to the electrical connections. We applied wire-bonding to make electrical connections between the filter device and the test setup. We used both wedge and ball bond alternatives and optimized bond parameters, i.e., ultrasonic power, force, time and work holder temperature. The pad structure used in the devices got damaged most of the time while making wire-bond applications. The majority of the limited number of visually successful wire-bond connections showed leakage resistance to the substrate in the range of 10Ω - $100k\Omega$. After many trials and optimization efforts, we concluded that the nitride isolation layer on top of the substrate is sensitive to the wire-bond process. As a solution, we proposed to use a probe station instead of a wire-bonding approach. Repeated tests showed that probed contacts do not have any leakage resistance.

The second major problem was the early collapsing of the devices at DC bias voltages lower than the calculated collapse voltage. We have checked out the same device types on different chips to determine it is a fabrication related issue. In addition to the low collapse voltage problem, varying collapse voltages were observed over the same sized resonators. Based on these findings, we suspected the residual oxide below the moving plate. The PolyMUMPs process includes the sacrificial layer removal by introducing 2 minutes of HF release followed by the supercritical CO₂ drying process. It turned out that the duration of the HF release process was not enough to dissolve the Oxide₂ layer in our design. Even if we followed the design rule of sacrificial layer release holes that need to be placed at less than 30 μ m spacing, the clamped periphery of the resonators could prevent adequate oxide removal. A solution to this problem is to apply an additional HF release process. In our case, we kept our chips under HF solution for 10 minutes. Then, the supercritical CO₂ drying process was applied to

prevent stiction of the moving plates. After the post-processes mentioned above, we verified that the early and irregular collapse problems were solved.

In the early phases of our measurements, we connected the coupled resonator under test to a carrier board with bias tees included. Wire-bond connections between the DUT and the carrier board are shown in Fig. 6.2. A photo of the carrier board is also given in Fig. 6.3. The carrier board was placed inside a

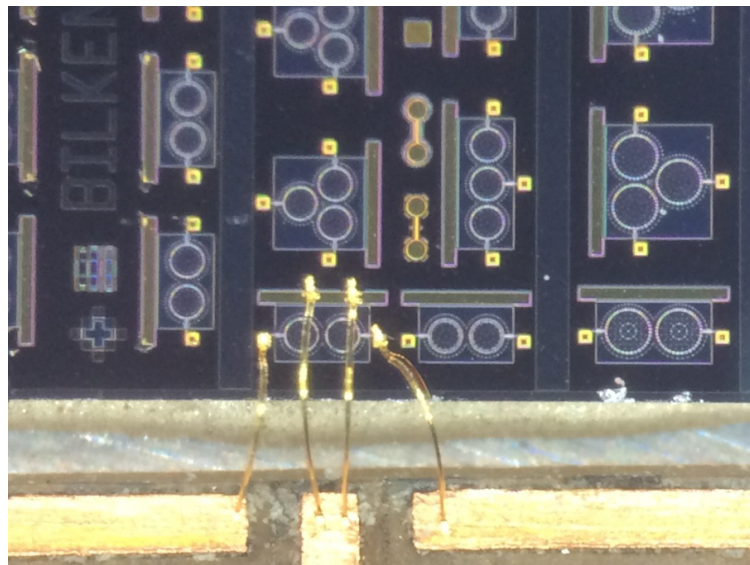


Figure 6.2: Photo of a coupled-resonator unit wire-bonded to a carrier board.

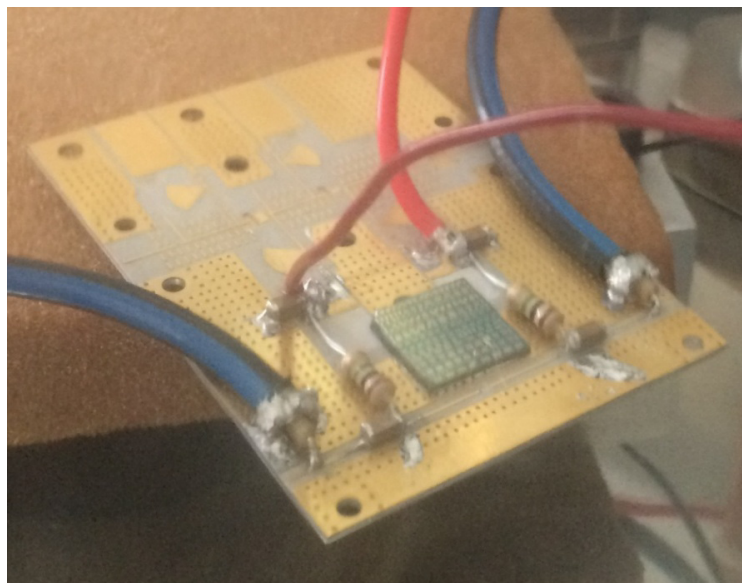


Figure 6.3: Photo of the carrier board including the bias tees and coaxial connections.

NANOVAK³ NVSS-600 vacuum chamber with a 10^{-7} Torr pressure level and several electrical feed-throughs, as shown in Fig. 6.4.

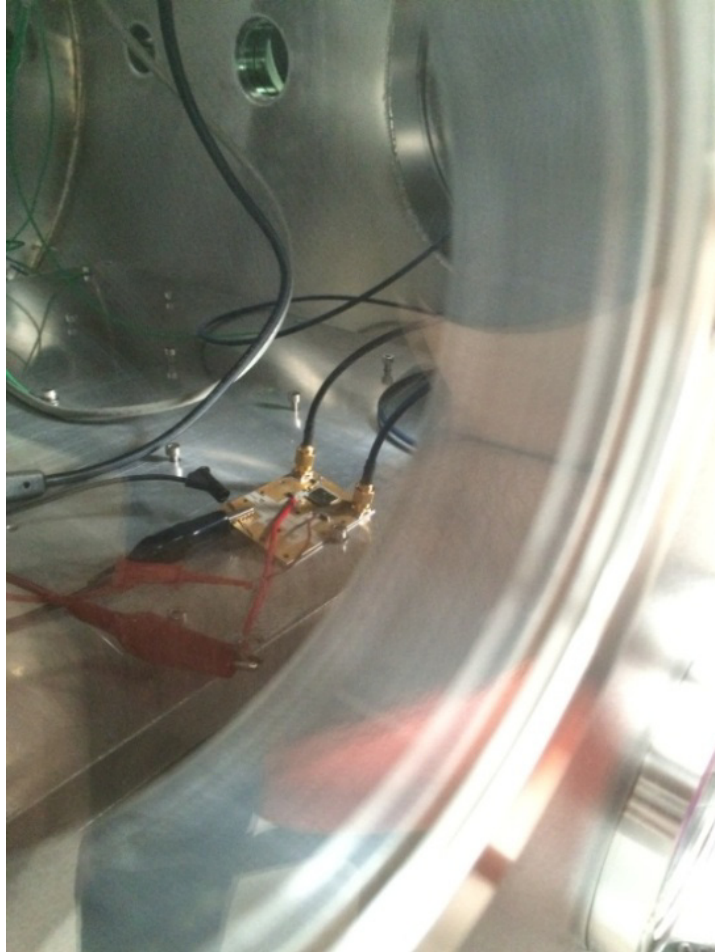


Figure 6.4: Photo of the carrier board inside a vacuum chamber.

In order to carry out the measurements without the need for wire-bond application, we connected the device to a test board via a probe station following the DC bias tests, as shown in Fig. 6.5. A close view of the chip under the probe is given in Fig. 6.6. The test board includes a series resistor at the input to provide matched source impedance and a two-stage trans-impedance amplifier (TIA) at the output to drive a 50Ω . The schematic of the test board is given in Fig. 6.7. The overall test unit was placed inside the vacuum chamber. A network

³NANOVAK, Inc., Ankara, Turkey, www.nanovak.com.tr

analyzer was used for the S-parameter measurements, while the DC biases were applied on both resonators. The interconnection between the test board and the network analyzer was made through the SMA feed-through connectors on the vacuum chamber.

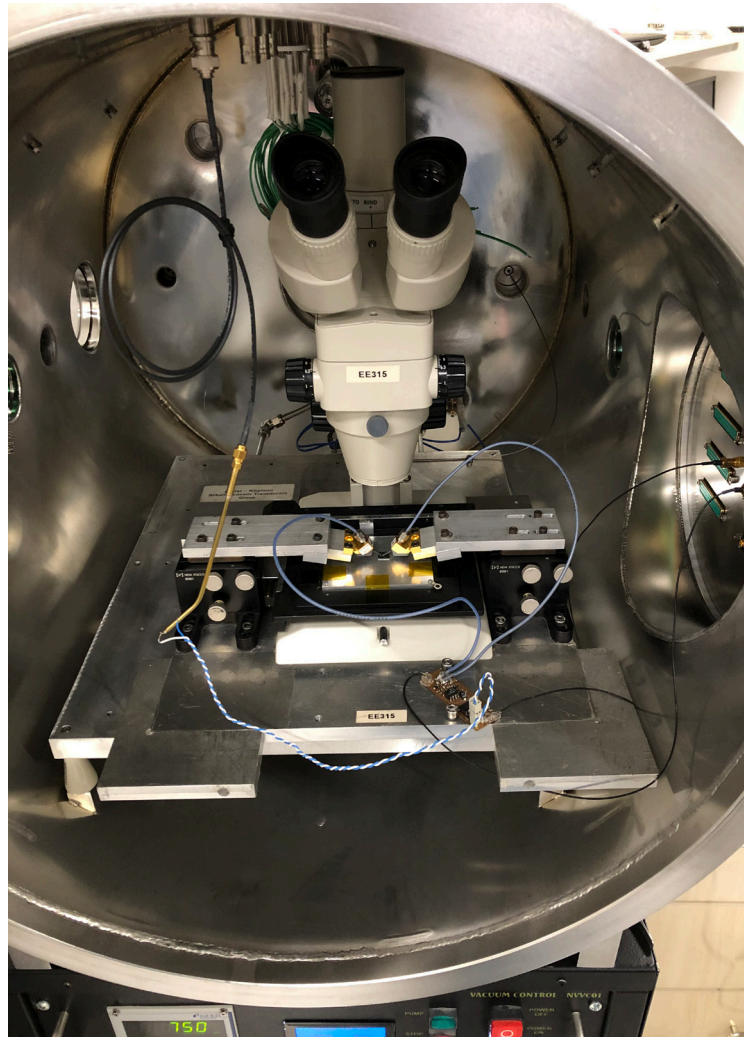


Figure 6.5: Photo of a coupled-resonator unit connected to a test board through a probe station. The test setup is placed inside a vacuum chamber.

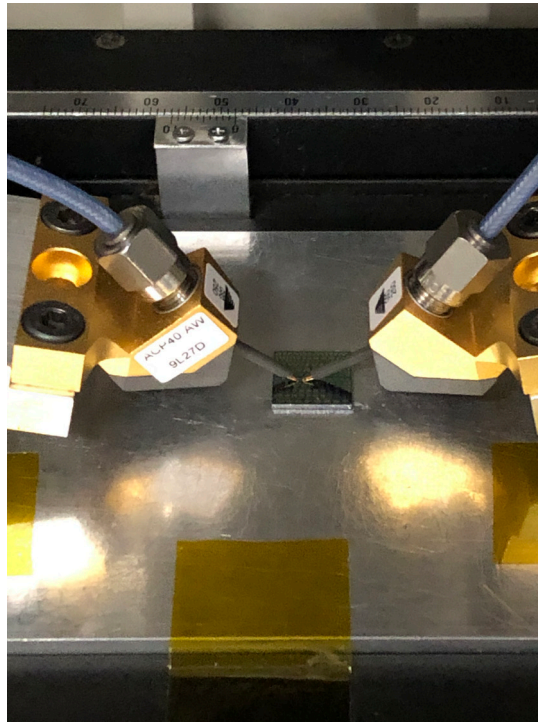


Figure 6.6: Photo of a coupled-resonator unit under probe station.

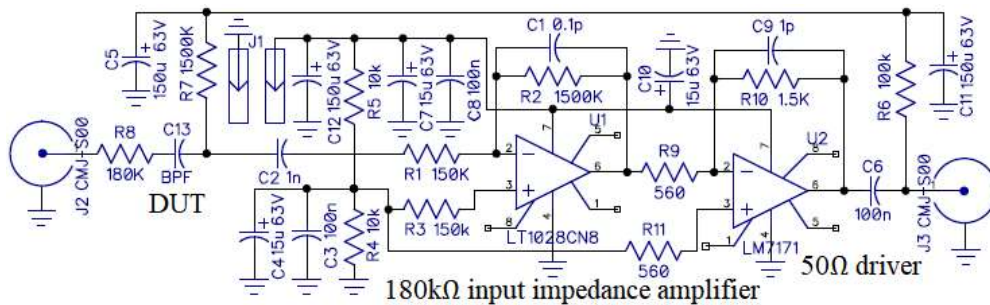


Figure 6.7: Schematic diagram of the test board.

6.2 Measurement Results

S-parameters of the test unit under vacuum are measured using a $50\ \Omega$ network analyzer. As explained in the test setup section, most of the devices showed early collapse behavior before the post-processing. The S-parameter response of such a coupled-resonator unit (device #1) is plotted in Fig. 6.8. The designed dimensions of this device are listed in Table 6.1. The applied bias voltage is 5V,

and the measured collapse voltage is $\sim 7V$, where the calculated collapse voltage is $\sim 25V$. The bandwidth measured is much less than the model expectations. The residual oxide problem is responsible for this deviation from the theoretical results.

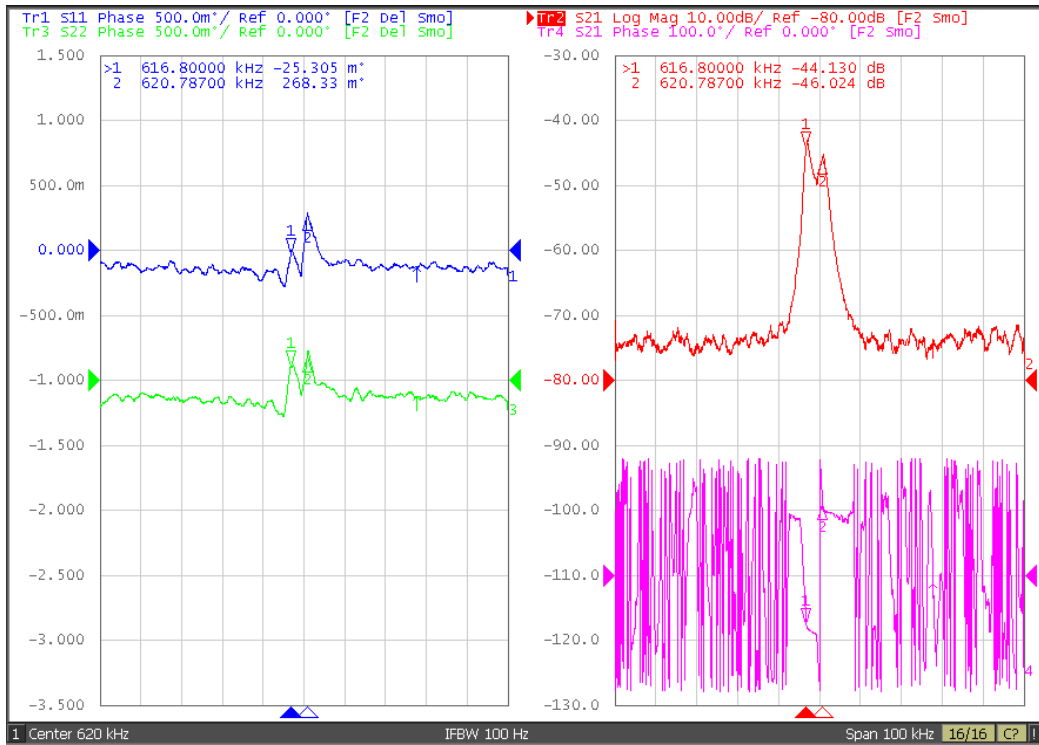


Figure 6.8: S-parameter measurement results of the device #1.

Resonator radius, a	100 μm
Electrode radius, a_o	80 μm
Plate thickness, t_m	1.5 μm
Gap height, t_g	750 nm
Overlap ratio, α	0.1

Table 6.1: Design dimensions of the device #1.

The next device measured has a closer collapse voltage to the expected value. The bias voltage applied is 18V. The design parameters are listed in Table 6.2. Measured S-parameters of this coupled-resonator unit is given in Fig. 6.9. The

Resonator radius, a	100 μm
Electrode radius, a_o	80 μm
Plate thickness, t_m	1.5 μm
Gap height, t_g	750 nm
Overlap ratio, α	0.075

Table 6.2: Design dimensions of the device #2.

dynamic range of the measurements is mainly limited by the impedance mismatch and the input power level. To make this coupled-resonator device a

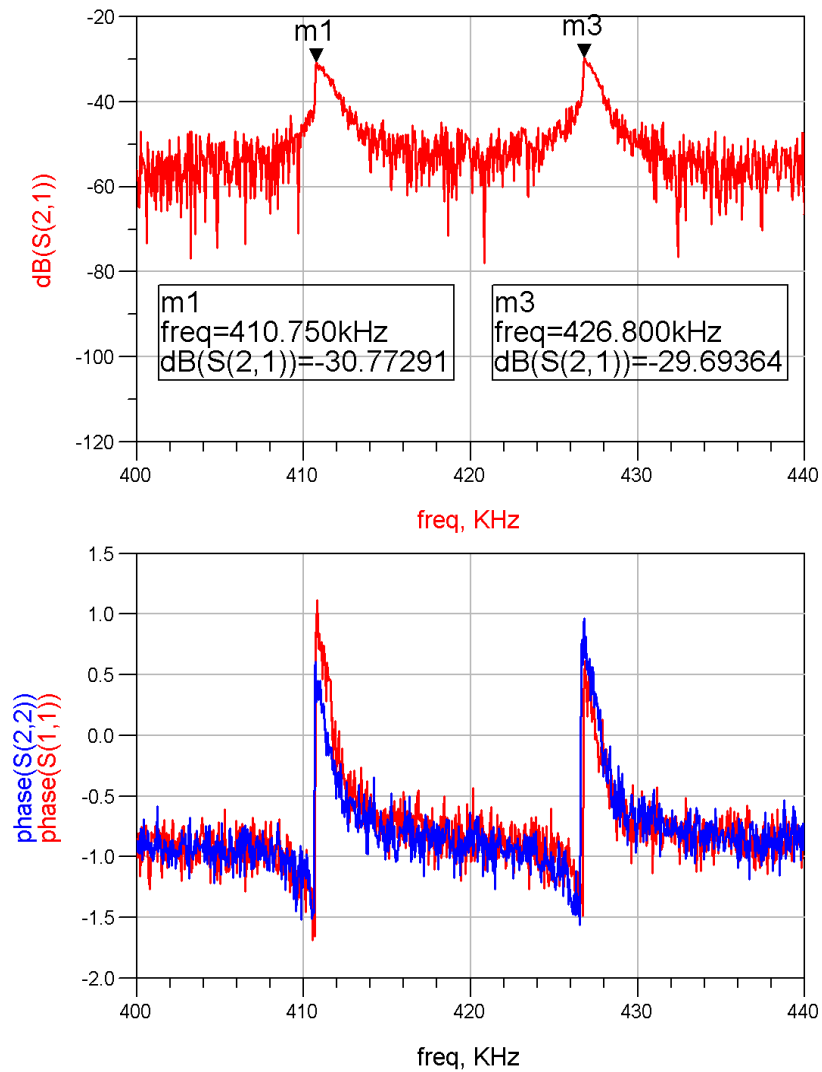


Figure 6.9: S-parameter measurement results of the device #2.

bandpass filter with 420kHz center frequency and 16kHz bandwidth, we need source and load impedances of 180k Ω under 18V DC bias. Using a 50 Ω system results in \sim 60dB overall mismatch loss, resulting in a poor measurement signal-to-noise ratio. The input power level of the network analyzer should be kept low in order to avoid large displacements due to the high-Q nature of the resonators under vacuum conditions. -55 dBm input power was applied, and 10Hz IF bandwidth was used in the network analyzer measurements.

After applying post-processes regarding the removal of the residual oxide and using the test board shown in Fig. 6.7 for proper impedance matching, we achieved the expected measurement results. Table 6.3 lists the measured average dimensions of the device #3 under test. S-parameter simulation results under DC bias voltages between 16 V and 22 V in 2 V steps are plotted in Fig. 6.10. There

Resonator radius, a	98 μm
Electrode radius, a_o	80 μm
Plate thickness, t_m	1.6 μm
Gap height, t_g	700 nm
Overlap ratio, α	0.043

Table 6.3: Measured dimensions of the device #3.

is a frequency shift to lower frequencies under increasing VDC, as expected. Corresponding measurement results of the device #3 are given in Fig. 6.11. We carried out the measurements under a custom-made probe station that fits in the vacuum chamber, as shown in Fig. 6.5. This approach brings the coaxial cable connection requirement between the probe station and the test board. The capacitance of this coaxial cable connection deteriorates the SNR of the measurements. In addition, the gap height variations between the resonators cause asymmetry in the transmission response. We observed a device characteristic that complies with the simulation results considering the tolerances of the material properties and the structural differences between the

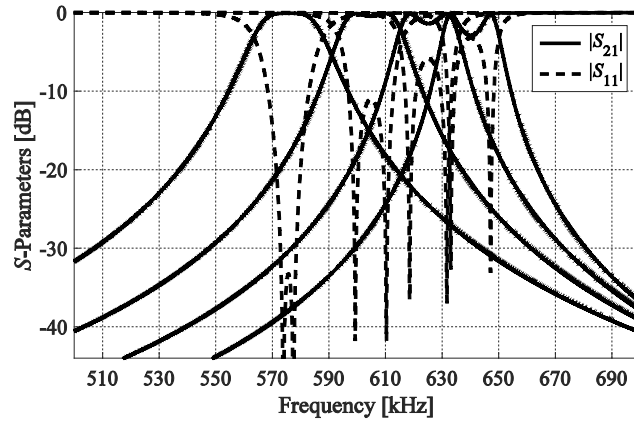


Figure 6.10: $|S_{21}|$ (solid line) and $|S_{11}|$ (dashed line) simulation results of the sample coupled-resonator device #3 for $V_{DC} = 16$ V up to 22 V in 2 V steps (from right to left) under vacuum.

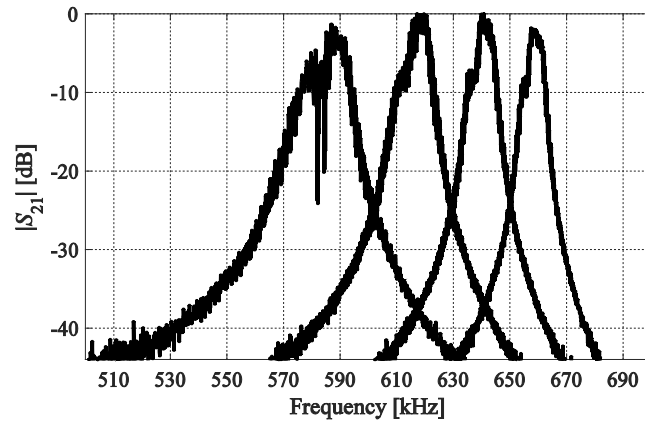


Figure 6.11: Measurement results of $|S_{21}|$ transmission characteristics of the sample coupled-resonator device #3 for $V_{DC} = 16$ V up to 22 V in 2 V steps (from right to left) under vacuum.

model assumptions and the PolyMUMPs process. We have verified that the model outcome matches the FEM simulations under various dimensional parameters and DC bias conditions. A dedicated process where a flat vibrating plate is produced is instrumental for improved precision in performance predictions.

Chapter 7

Conclusions

We proposed and experimentally validated modeling and design approaches for a mechanically coupled clamped circular plate resonator structure without a separate mechanical coupling element. Low mechanical complexity and high reliability were the main motivations behind the choice of this structure.

The usual practice presented in the literature is to analyze fabricated coupled MEMS resonators using FEM and tune the model parameters accordingly for specific dimensions, bias voltage, and material parameters. This approach makes designing a coupled-resonator filter based on electrical specifications very difficult. We developed a physics-based lumped element equivalent circuit model, which provides insight, accurate and fast simulation results. The model revealed the practical limitations on the center frequency, bandwidth, and termination impedance. We also derived a formula that relates the ratio of the termination impedance to the center frequency for polysilicon material under the specified conditions: $a_0=0.8a$, $V_{DC}/V_{re}=0.9$, $t_{ge}=100$ nm, $a/t_m=10$, and $\alpha=0.01$. Using the provided design procedure, one can determine whether this coupled-resonator structure satisfies the required filter specifications.

PolyMUMPs process was used for the experimental verification of the model. An optimum design could not be implemented due to the process limitations, such as the gap height, plate thickness, and sacrificial layer release holes. Although the process enforced some structural differences from the proposed model, the measurement results proved the validity of the developed model. Dedicated production processes in which uniform vibration plates can be implemented are helpful to have better-performing resonators.

As future work, higher-order bandpass filters based on in-line or cyclic connections [23, 40] of more than two clamped circular plate resonators can be designed using the given model approach. Cross-coupling between the non-neighboring resonators can also be implemented by placing additional mechanical paths made of a series of in-line coupled resonators.

BIBLIOGRAPHY

- [1] Mason W P 1939 *Electrical and electromechanical system employing magnetostrictive devices* Patent No. US2170206A
- [2] Doelz M L 1952 *Electromechanical filter* Patent No. US2615981A
- [3] George R W 1956 Electromechanical filters for 100-kc carrier and sideband selection *Proc. IRE* **44** 14–18
- [4] Hathaway J C and Babcock D F 1957 Survey of mechanical filters and their applications *Proc. IRE* **45** 5–16
- [5] Fowler P H 1965 *Piezoelectric filter* Patent No. US3189851A
- [6] Johnson R A, Borner M and Konno M 1971 Mechanical filters-A review of progress *IEEE Trans. Sonics Ultrason.* **18** 155–170.
- [7] Johnson R A 1983 *Mechanical Filters in Electronics* (New York: John Wiley & Sons)
- [8] Linder C, Paratte L, Gretillat M-A, Jaecklin V P and de Rooij N F 1992 Surface micromachining *J. Micromech. Microeng* **2** 122–132
- [9] Howe R T, Boser B E and Pisano A P 1996 Polysilicon integrated microsystems: technologies and applications *Sens. Actuators A: Phys.* **56** 167–177
- [10] Bustillo J M, Howe R T and Muller R S 1998 Surface micromachining for microelectro-mechanical systems *Proc. IEEE* **86** 1552–1574
- [11] Ayazi F and Najafi K 2000 High aspect-ratio polysilicon micromachining technology *Sens. Actuators A: Phys.* **87** 46–51
- [12] Lin L, Howe R T and Pisano A P 1998 Microelectromechanical filters for signal processing *J. Microelectromech. Syst.* **7** 286–294
- [13] Wang K and Nguyen C T-C 1999 High-order medium frequency micromechanical electronic filters *J. Microelectromech. Syst.* **8** 534–556

- [14] Jing Q, Luo H, Mukherjee T, Carley L R and Fedder G K 2000 CMOS micromechanical bandpass filter design using a hierarchical MEMS circuit library *Proc. 13th IEEE Int. Conf. Micro Electro Mech. Syst.* 187–192
- [15] Bannon F D, Clark J R and Nguyen C T-C 2000 High-Q HF microelectromechanical filters *IEEE J. Solid-State Circuits* **35** 512–526
- [16] Motiee M, Mansour R R and Khajepour A 2006 Novel MEMS filters for on-chip transceiver architecture, modeling and experiments *J. Micromech. Microeng.* **16** 407–418
- [17] Pourkamali S and Ayazi F 2005 Electrically coupled MEMS bandpass filters: part I: with coupling element *Sens. Actuators A: Phys.* **122** 307–316
- [18] Pourkamali S and Ayazi F 2005 Electrically coupled MEMS bandpass filters: part II. without coupling element *Sens. Actuators A: Phys.* **122** 317–325
- [19] Galayko D, Kaiser A, Legrand B, Buchailot L, Combi C and Collard D 2006 Coupled-resonator micromechanical filters with voltage tuneable bandpass characteristic in thick-film polysilicon technology *Sens. Actuators A: Phys.* **126** 227–240
- [20] Li S-S, Lin Y-W, Ren Z and Nguyen C T-C 2006 Disk-array design for suppression of unwanted modes in micromechanical composite-array filters *Proc. 19th IEEE Int. Conf. MEMS, Tech. Dig.* 866–869
- [21] Li S-S, Lin Y-W, Ren Z and Nguyen C T-C 2007 A micromechanical parallel-class disk-array filter *Proc. IEEE Int. Freq. Control Symp. Joint 21st Eur. Freq. Time Forum* 1356–1361
- [22] Shalaby M M, Abdelmoneum M A and Saitou K 2009 Design of spring coupling for high-Q high-frequency MEMS filters for wireless applications *IEEE Trans. Ind. Electron.* **56** 1022–1030
- [23] Greywall D and Busch P 2002 Coupled micromechanical drumhead resonators with practical application as electromechanical bandpass filters *J. Micromech. Microeng.* **12** 925–938

- [24] Acar M A, Atalar A, Yilmaz M and Köymen H 2021 Mechanically coupled clamped circular plate resonators: modeling, design and experimental verification *J. Micromech. Microeng.* **31** 105002
- [25] Köymen H, Atalar A, Aydogdu E, Kocabas C, Oguz K, Olcum S, Ozgurluk A and Unlugedik A 2012 An improved lumped element nonlinear circuit model for a circular CMUT cell *IEEE Trans. Ultrason., Ferroelectr., Freq. Control* **59** 1791–1799
- [26] Wang K, Bannon III F D, Clark J R and Nguyen C T-C 1997 Q-enhancement of micromechanical filters via low-velocity spring coupling *Proc. IEEE Int. Ultrason. Symp.* **1** 323–327
- [27] Greenspan M 1979 Piston radiator: Some extensions of the theory *J. Acoust. Soc. Am.* **65** 608–621
- [28] Timoshenko S and Woinowsky-Krieger S 1959 *Theory of Plates and Shells, 2nd ed.* (New York: McGraw-Hill)
- [29] Mason W P 1942 *Electromechanical Transducers and Wave Filters* (New York: D. Van Nostrand)
- [30] Leissa A W 1969 *Vibration of Plates* (NASA SP-160, US Government Printing Office)
- [31] Kelly P 2013 *Solid Mechanics Lecture Notes Part II*
http://homepages.engineering.auckland.ac.nz/~pkel015/SolidMechanicsBooks/Part_II/06_PlateTheory/06_PlateTheory_08_Vibrations.pdf
- [32] Bircumshaw B, Liu G, Takeuchi H, King T J, Howe R, O'Reilly O and Pisano A 2003 The radial bulk annular resonator: towards a 50 Ω RF MEMS filter *Proc. 12th Int. Conf. Solid-State Sens., Actuators, Microsyst.* **1** 875–878
- [33] Demirci M U and Nguyen C T-C 2006 Mechanically corner-coupled square microresonator array for reduced series motional resistance *J. Microelectromech. Syst.* **15** 1419–1436
- [34] Clark J R, Pai M, Wissman B, He G and Hsu W-T 2006 Parallel-coupled square-resonator micromechanical filter arrays *Proc. Int. Freq. Control Symp. Expos.* 485–490

- [35] Nguyen C T-C 2007 MEMS technology for timing and frequency control *IEEE Trans. Ultrason., Ferroelectr., Freq. Control* **54** 251–270
- [36] Pourkamali S, Ho G K and Ayazi F 2007 Low-impedance VHF and UHF capacitive silicon bulk acoustic wave resonators—part I: concept and fabrication *IEEE Trans. Electron Devices* **54** 2017–2023
- [37] Forouzanfar S, Mansour R and Abdel-Rahman E 2012 Lorentz force transduction for RF micromechanical filters *J. Micromech. Microeng.* **22** 035018
- [38] Ziaei-Moayyed M and Howe R T 2010 Higher-order dielectrically transduced bulk-mode ring resonator with low motional resistance *IEEE Int. Freq. Cont. Symp.* 19–24
- [39] Hung L-W 2011 *High-Q low-impedance MEMS resonators, Ph.D. dissertation* <http://www2.eecs.berkeley.edu/Pubs/TechRpts/2012/EECS-2012-218.pdf>.
- [40] Chivukula V B and Rhoads J F 2010 Microelectromechanical bandpass filters based on cyclic coupling architectures *J. Sound Vibrat.* **329** 4313–4332

Appendix A

ANSYS Code for the Simulation of Mechanically Coupled Clamped Circular Plate Resonators

We performed FEM simulations to extract the coupling parameters between the clamped circular plate resonators. ANSYS is used for the script-based configuration capability, which allows seamless parameter sweeps for many design variations.

The following code was used for the coupled polysilicon resonator simulation with parameters: $a_o=100\ \mu\text{m}$, $a=80\ \mu\text{m}$, $t_g=750\ \text{nm}$, $t_m=1.5\ \mu\text{m}$, $\alpha=0.075$, and $V_{\text{DC}}=18\ \text{V}$.

```
FINISH
/CLEAR,NOSTART
/prep7

pi = 4*ATAN(1)
e_poly          = 158e3
dens_poly       = 2329e-18
poiss_poly      = 0.22

!Physical Dimensions
radius1 = 100
radius2 = 100
tg = 0.75
tm = 1.5
overlap_ratio = 0.15
electrode_ratio = 0.80

!Define Elements
ET,1,SOLSH190
KEYOPT,1,8,1 ! Write Layer Results
```

```

!Material Properties
mp, ex, 1, e_poly           !Plate Material is Polysilicon
mp, dens, 1, dens_poly
mp, nuxy, 1, poiss_poly
mp, dmpr, 1, 0.001

!Setting Up the Structure
CYL4,0,0,radius1,-45,0,45,tm/4
CYL4,0,0,radius1,45,0,135,tm/4
CYL4,0,0,radius1,135,0,225,tm/4
CYL4,0,0,radius1,225,0,315,tm/4

BLOCK, (1-overlap_ratio/2)*radius1,radius1,-
radius1,radius1,0,tm/4
vsbv,all,5,,delete,delete

allsel
wpoffs, (1-overlap_ratio/2)*radius1,0,0
CSWPLA,12,0
csys,12
vsymm,x,all,,,0,0,0

allsel
vgen,4,all,,,0,0,tm/4,0,0,0

allsel
vglue,all
allsel

cm,membrane_volu,volu
allsel

csys,1
wpave,0,0,0

asel,s,loc,z,0
cm,source_area,area

allsel
asel,s,loc,z,tm
cm,target_area,area

!Area Mesh Setup
esize,2*tm
vatt,1,,1,
vsweep,membrane_volu,source_area,target_area
allsel
aclear,all
allsel

!Boundary Conditions
allsel

```

```

asel,s,ext
asel,u,loc,z,0
asel,u,loc,z,tm
csys,1
wpave,0,0,0
nsla,s,1
cm,clamped_nodes,node
d,all,UX,0
d,all,UY,0
d,all,UZ,0
allsel

csys,1
nset,s,loc,z,0
nset,r,loc,x,0,electrode_ratio*radius1

cm,cond1,node
csys,0
! Place TRANS126 Elements
EMTGEN, 'cond1','memb_trans126','ground1', 'uz', -tg, 0,1
allsel

wpoffs,(2-overlap_ratio)*radius1,0,
CSWPLA,11,1,1,1,
csys,11
nset,s,loc,z,0
nset,r,loc,x,0,electrode_ratio*radius1

cm,cond2,node
csys,0
! Place TRANS126 elements
EMTGEN, 'cond2','memb_trans126_2','ground2', 'uz', -tg, 0,1
allsel

D,ground1,UX,0
D,ground1,UY,0
D,ground1,UZ,0
D,ground2,UX,0
D,ground2,UY,0
D,ground2,UZ,0

nset, s,node,, cond1
cp,1,VOLT,all !Couple Top Electrode
NTOP1=ndnext(0)
allsel

nset, s,node,, cond2
cp,2,VOLT,all !Couple Top Electrode
NTOP2=ndnext(0)
allsel

nset,s,node,,ground1
nset,a,node,,ground2
cp,3,VOLT,all

```

```

BTOP=ndnext(0)
D,BTOP,VOLT,0

csys,0
wpave,0,0,0

allsel
FINISH

Vdc = 18

!Static Solution Under DC Bias
/SOLU
BCSOPTION,,DEFAULT
ANTYPE,STATIC
NLGEOM, OFF
PSTRES,ON

D, NTOP1, VOLT, Vdc
D, NTOP2, VOLT, Vdc

autots,on
cnvtol,u
lnsrch,on
neqit,500
allsel, all, all

SOLVE
FINISH

!Modal Analysis Option
/SOLU
ANTYPE,MODAL
PSTRES,ON
MODOPT,UNSYM,2
allsel, all, all
SOLVE
FINISH

Vac = 0.001
fstart = 510.0e3
fstop = 535.0e3
points = 250

!AC Analysis Option
/SOLU
BCSOPTION,,DEFAULT
DDELE, NTOP1, VOLT
DDELE, NTOP2, VOLT
ANTYPE,3
PSTRES,ON
HARFRQ,fstart,fstop,
NSUBST,points,
KBC,1

```

```
D, NTOP1, VOLT, Vac
D, NTOP2, VOLT, 0
```

```
allsel, all, all
SOLVE
FINISH
```

```
/POST26
NSOL, 2, NTOP1, VOLT,
STORE, MERGE
XVAR, 1
PLVAR, 2,
```

```
NSOL, 3, NTOP2, VOLT,
STORE, MERGE
XVAR, 1
PLVAR, 3,
```

```
csys, 1
midnode1=NODE(0, 0, 0)
csys, 11
midnode2=NODE(0, 0, 0)
```

```
NSOL, 4, midnode1, U, Z,
STORE, MERGE
XVAR, 1
PLVAR, 4,
```

```
NSOL, 5, midnode2, U, Z,
STORE, MERGE
XVAR, 1
PLVAR, 5,
```

```
FINISH
```

Appendix B

The Equivalent Circuit Model Implementation in ADS

We used Advanced Design System (ADS) circuit simulator to implement the developed model for the coupled-resonators introduced in this work. Fig. B.1 shows the small-signal filter schematic. Rpath and Cpar correspond to parasitic resistance and capacitance values due to the external connections. Their values need to be calculated for the specific measurement conditions.

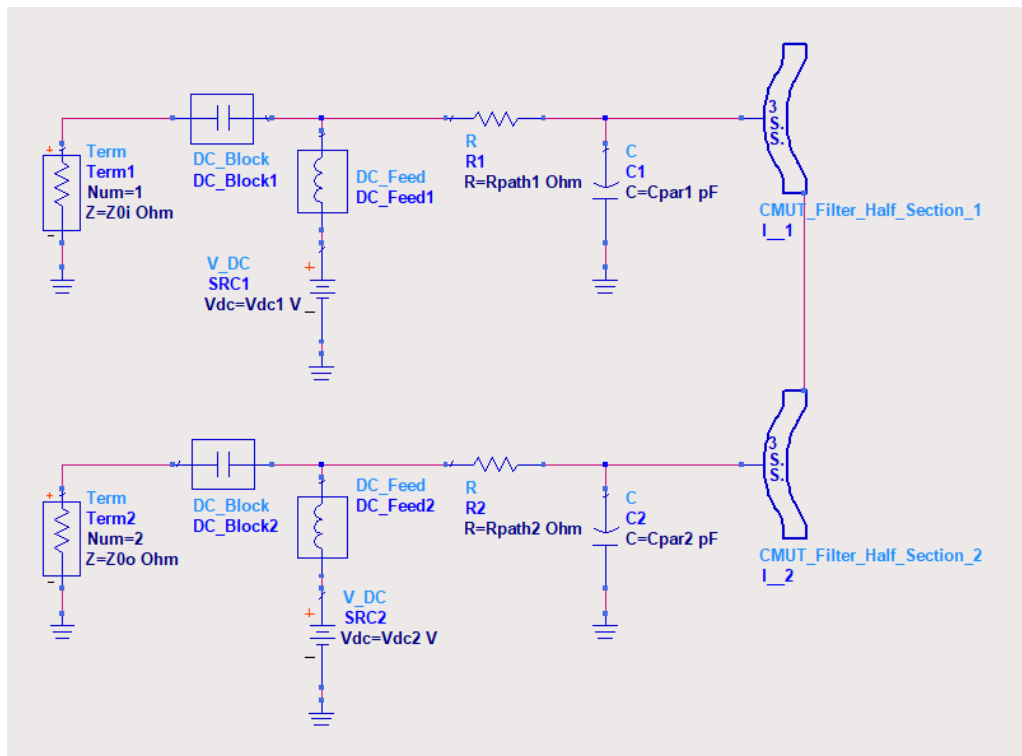


Figure B.1: ADS small-signal schematic setup for the coupled-resonator filter.

Each resonator is represented by a separate hierarchical component which includes the coupling effect. Details of this component are given in Fig. B.2, where the circuit parameters are calculated as explained in Section 3.

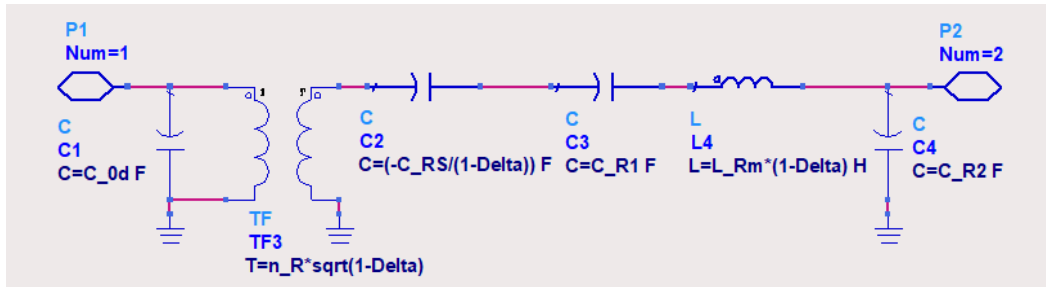


Figure B.2: The half section of the coupled-resonator implemented in ADS.